Supporting Information for

Pentavalent Manganese Luminescence: Designing Narrow-Band Near-Infrared Light-Emitting Diodes as Next-Generation Compact Light Source

Veeramani Rajendran,[†,‡] Kuan-Chun Chen,[†] Wen-Tse Huang,[†] Natalia Majewska,[§] Tadeusz Leśniewski,[§] Maciej Grzegorczyk,[§] Sebastian Mahlik,[§] Grzegorz Leniec,[&] Sławomir Maksymilian Kaczmarek,[&] Wei Kong Pang,[#] Vanessa K. Peterson,[#,ϕ,] Kuang-Mao Lu,[⊥] Ho Chang,[‡,*] and Ru-Shi Liu[†,*]*

†Department of Chemistry, National Taiwan University, Taipei 106, Taiwan
‡Department of Mechanical Engineering and Graduate Institute of Manufacturing Technology, National Taipei University of Technology, Taipei 106, Taiwan
§Institute of Experimental Physics, Faculty of Mathematics, Physics, and Informatics, University of Gdansk, Wita Stwosza 57, 80-308 Gdańsk, Poland
&Department of Technical Physics, Department of Mechanical Engineering and Mechatronics, West Pomeranian University of Technology Szczecin, al. Piastow 48, 70-311 Szczecin, Poland
#Institute for Superconducting and Electronic Materials, University of Wollongong, Squires Way, North Wollongong, New South Wales 2500, Australia
ϕAustralian Centre for Neutron Scattering, Australian Nuclear Science and Technology Organisation, Sydney, New South Wales 2232, Australia
⊥Everlight Electronics Co., Ltd., New Taipei City 238, Taiwan

***Corresponding authors**
vanessa.peterson@ansto.gov.au (Vanessa K. Peterson); f10381@ntut.edu.tw (Ho Chang); rsliu@ntu.edu.tw (Ru-Shi Liu)

Experimental Methods

Reagents

Calcium carbonate ($CaCO_3$, 99.9%) was purchased from Showa Chemical, Japan. Zinc oxide (ZnO, 99.9%) was obtained from J. T. Baker, Fisher Scientific. Gallium oxide (Ga_2O_3, 99.9%) was obtained from Gredmann, Taiwan, and magnesium oxide (MnO, 99.9%) was purchased from Merck, Germany.

Synthesis of $Ca_{14}Zn_6Ga_{10-x}O_{35}$:$x$$Mn^{4+}$ (x = 0, 0.3, 0.5, 1.0, 1.25, 1.5, and 3.0)

Stoichiometric amounts of starting precursors were weighed and ground using a mortar and pestle for 15 min to obtain a homogenous mixture. Mixtures were sintered at 1230 °C for 6 h in the air in an alumina crucible. Sintered samples were ground for characterization.

Characterization Techniques

Structural Investigations: A Bruker D2 phaser desktop diffractometer with CuKα radiation was used to collect X-ray powder diffraction (XRD) data for $Ca_{14}Zn_6Ga_{10-x}Mn_xO_{35}$ (x = 0, 0.3, 0.5, 1.0, 1.25, 1.5, and 3.0) at room temperature (RT) within the 2θ range 10–80°. RT synchrotron XRD (S-XRD) data were collected for $Ca_{14}Zn_6Ga_{10-x}Mn_xO_{35}$ (x = 0, 0.3, 0.5, 1.0, 1.25, 1.5, and 3.0) at beamline BL01C2 of the National Synchrotron Radiation Research Center (Taiwan) with the electron storage ring operating at 1.5 GeV with a beam current of 360 mA. The National Institute of Standards and Technology (NIST) standard reference material (SRM) LaB_6 660a was employed to determine the wavelength for S-XRD measurement as 0.77491(1) Å. RT high-resolution neutron powder diffraction (NPD) data for $Ca_{14}Zn_6Ga_{10-x}Mn_xO_{35}$ (x = 0, 0.3, 0.5, 1.0, 1.25, 1.5, and 3.0) were collected using the Echidna[1] instrument at the Open Pool Australian Light-water research reactor of the Australian Nuclear Science and Technology Organization. Data were collected within the 2θ range 4–164° with 1.62227(5) Å neutrons as determined using the NIST LaB_6 660b SRM. The International Centre for Diffraction Data structural database entry #ICDD 04-009-7303[2] was used as starting model for $Ca_{14}Zn_6Ga_{10-x}Ga_xO_{35}$ (x = 0, 0.3, 0.5, 1.0, 1.25, 1.5, and 3.0) refinement through Rietveld method within the academic Total Pattern Analysis Solutions (TOPAS) software (version 5.0).[3] To investigate the distribution of Mn at the Ga site and composition, two different approaches were adopted in this work. In one approach, Rietveld refinement was carried out using only NPD data due to better coherent length neutron scattering contrast between Ga and Mn.[4] The refined parameters in the starting model included lattice parameters, atomic positions, and isotropic atomic displacement parameters. The total amount of Mn in the model was unconstrained and the site occupancy factors of Mn at Ga sites were constrained to sum to the maximum, (Ga, Mn)1 = 1, (Ga, Mn)2 = 1, (Ga, Mn)3 = 1 and

(Ga, Mn)4 = 0.5. In another approach, joint Rietveld refinement was performed simultaneously against both S-XRD and NPD data, and the total amount of Mn in the model was constrained to maintain the nominal chemical composition. The refined parameters in the structural model included lattice parameters, atomic positions, site occupancy factors, and isotropic atomic displacement parameters. Site occupancy factors for Mn substitution at Ga sites were handled using constraints for Ga1–Ga4 sites as follows:

For x = 0.5: Ga1 = a, Mn1 = 1−a, Ga2 = 2.375/1.5−a/6−b/6−c/1.5, Mn2 = 1−(2.375/1.5−a/6−b/6−c/1.5), Ga3 = b, Mn3 = 1−b, Ga4 = c, Mn4 = 0.5−c.

Similarly, for x = 1.0, Ga2 = 2.25/1.5−a/6−b/6−c/1.5, Mn2 = 1−(2.25/1.5−a/6−b/6−c/1.5); for x = 1.25, Ga2 = 2.185/1.5−a/6−b/6−c/1.5, Mn2 = 1−(2.185/1.5−a/6−b/6−c/1.5); for x = 1.5, Ga2 = 2.125/1.5−a/6−b/6−c/1.5, Mn2 = 1−(2.125/1.5−a/6−b/6−c/1.5); for x = 3.0, Ga2 = 1.75/1.5−a/6−b/6−c/1.5, Mn2 = 1−(1.75 /1.5−a/6−b/6−c/1.5).

Atomic displacement parameters were constrained to be the same for atoms at the same site. The Visualization for Electronic and Structural Analysis[5] software version 3.5.5 was used to visualize crystal structures and a distortion index (D) for polyhedral was calculated as defined by Baur in Equation (S1).[6]

$$\mathrm{D} = \frac{1}{\mathrm{n}}\sum_{\mathrm{i}=1}^{\mathrm{n}} \frac{|\, l_i - l_{av} \,|}{l_{av}}, \qquad \text{(S1)}$$

where l_i is the distance from the central atom to the i^{th} coordinating atom and l_{av} is the average bond length.

Luminescence Investigations: RT photoluminescence excitation (PLE) spectra of visible (red) emission were obtained using a FluoroMax-4P spectrofluorometer (Horiba Scientific) equipped with a 150 W xenon lamp as an excitation source and an R928 Hamamatsu photomultiplier detector in the range 250–850 nm. NIR emission spectra were obtained using a custom setup consisting of a 150 W xenon lamp (LOT quantum design) coupled with a grating monochromator (Omni-λ 1509) excitation source operating in the range 250–1000 nm and an Avalanche Photodetector APD110C/M operating in the range 900–1700 nm. Temperature- and pressure-dependent red emission spectra were obtained using an Andor SR-750-D1 spectrometer equipped with a charge-coupled device (CCD) camera (DU420A-OE) operating between 350 and 1000 nm. Temperature- and pressure-dependent NIR emission spectra were measured using an Andor SR-500i-D1

spectrometer equipped with a CCD camera (DU490A-1.7) operating between 600 and1700 nm. A LED with maximum emission at 475 nm and a diode-pumped solid-state neodymium-doped yttrium aluminum garnet (YAG:Nd) laser with a 473 nm emission were used as excitation sources for temperature- and pressure-dependent measurements, respectively.

Decay profiles of red emissions were measured using a time-resolved spectroscopy[7] apparatus consisting of a PG 401/SH optical parametric generator pumped by a PL2251A pulsed YAG:Nd laser (EKSPLA) with detection using a 2501S grating spectrometer (Bruker Optics) combined with a C4334-01 streak camera (Hamamatsu). NIR emission decay was measured using a custom setup consisting of a square-shaped light pulse generator with 100 *ms* duration and approximately 100 *ns* fall time using an Avalanche Photodetector APD110C/M operated in the range of 900–1700 nm and a National Instrument Data Acquisition module.

Samples for time-resolved red emission luminescence measurements were cooled using an APD Cryogenics closed-cycle DE-202 optical cryostat, enabling temperature between 30 and 470 K. Temperature control during measurement of red and NIR emission spectra was achieved using a THMS600 Linkam stage temperature controller combined with an LNP95 liquid nitrogen cooling pump system, enabling temperature control in the 100–600 range K. High-pressure luminescence measurements were performed in a screw-driven Merrill–Bassett-type diamond anvil cell with a 0.5 mm diamond culet diameter[8]. The gasket for the pressure chamber was pre-indented to approximately 0.08 mm and a 0.2 mm diameter hole was drilled in the center. $KMgF_3$:0.5%Eu^{2+} was used as a pressure sensor[9] with a polydimethylsiloxane oil pressure transmitting medium.

A Hamamatsu Quantaurus QY plus UV-NIR absolute quantum yield spectrometer C13534 machine configured with a high-power Xe lamp at a fixed excitation wavelength of 475 ± 25 nm was used to measure the internal quantum efficiency of $Ca_{14}Zn_6Ga_{10-x}Ga_xO_{35}$ (x = 0.3, 0.5, 1.0, 1.25, 1.50, and 3.0) samples. Absorption and absolute internal quantum yield are measured, with the estimation of external quantum efficiency from these being difficult and not determined. The integrating range is limited for the emission range of Mn^{4+} and Mn^{5+} to measure the absolute internal quantum efficiency separately.

Short-range Investigations: Mn *K*-edge X-ray absorption near-edge structure data were collected at beamline BL17C1 of the National Synchrotron Radiation Research Center in total fluorescence yield mode using a double-crystal Si(111) monochromator.

A conventional Bruker X-band E LEXSYS E500 CW spectrometer operating at 9.6 GHz and 0.6 mW microwave power was used to record EPR spectra in the range of 80–350 K. The first derivative of the absorption spectrum was measured as a function of an applied magnetic field, which varied from 0 to 1.4 mT. Static measurements of the magnetic susceptibility were performed using a Superconducting Quantum Interference Device (SQUID) with an EverCool Magnetic Property Measurement System (MPMS XL). Magnetic susceptibility (MS) was measured in two modes: Zero Field Cooling (ZFC) and Field Cooling (FC). Measurements were recorded in the range from 2 K to room temperature and magnetic field up to 30 kOe. Curie–Weiss and Bleaney–Bowers methods were used for a weak magnetic field H = 100 Oe to fulfill the condition H/kT << 1. Susceptibility data were corrected for sample holder diamagnetism and constituent atoms by Pascal's constants.[10] The EPR spectrum was obtained in arbitrary units where T_{CW} and J are only indicative of the nature and strength of paramagnetic interactions of half-spin ions such as Mn^{4+}, and all paramagnetic ions such as Mn^{5+} contribute to the MS as measured by SQUID. Therefore, the SQUID-measured MS might differ from the EPR-measured MS, affecting T_{CW} and J interaction parameters.

Temperature Dependent Photoluminescence (Arrhenius Equation)

The intensity I of Mn^{4+} and Mn^{5+} emissions at temperature T in Figure 4c is determined using Equation (S1).

$$\boldsymbol{I(T) = \frac{I(0)}{1 + A\exp\left(-\frac{E_A}{kT}\right)}}, \qquad \text{(S1)}$$

where k is Boltzmann's constant, $I(0)$ is the intensity at $T = 0$ K, and E_A is the activation energy for the non-radiative transition. A is a dimensionless constant equal to p_{nr}/p_r, where p_{nr} and p_r are the probability of non-radiative and radiative transitions, respectively. $1/p_r$ is equal to τ_0, which is the radiative lifetime of emission at low

temperatures.

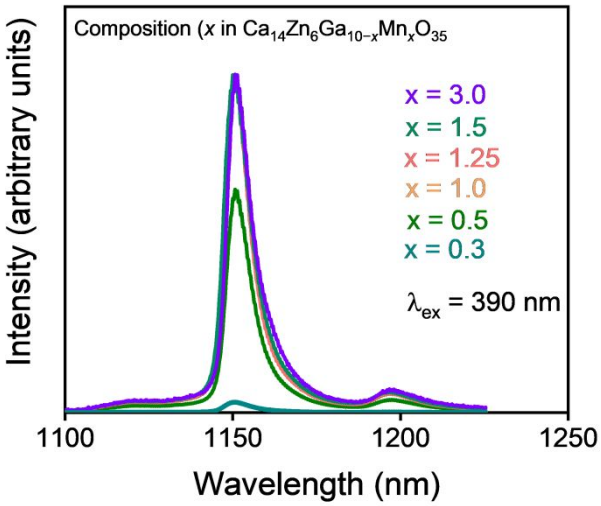


Figure S1. RT photoluminescence spectra of $Ca_{14}Zn_6Ga_{10-x}Mn_xO_{35}$ (x = 0.3, 0.5, 1.0, 1.25, 1.5, and 3.0) in the range 1100–1250 nm upon excitation at 390 nm.

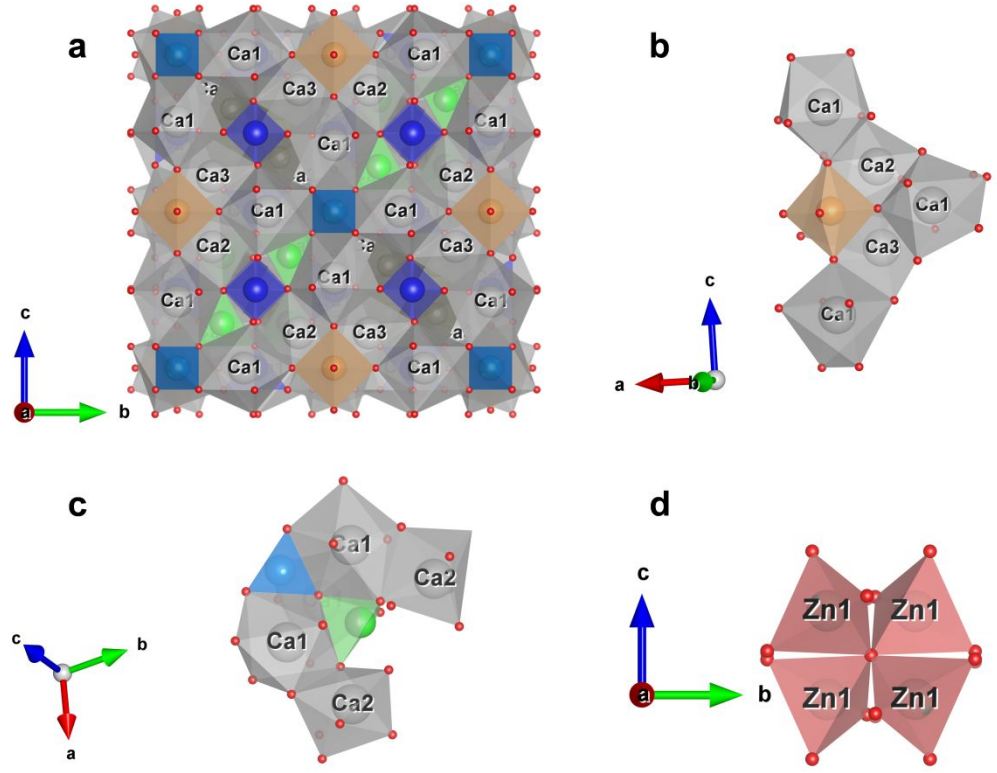


Figure S2. (a) Refined crystal structure model of $Ca_{14}Zn_6Ga_{10}O_{35}$ with space group of *F23* after joint Rietveld refinement (#ICDD 04-009-7303 is used as the initial structural model).[2] (b) Edge-sharing of Ca1 with Ca2 and Ca3 units. (c) Short-range structure of Ca1 units connected through a common corner. d, Group of four vertex-linked tetrahedral units of Zn. Light blue, violet, orange, and green polyhedra and spheres are Ga. Red is O.

Figure S2a shows the crystal structure of $Ca_{14}Zn_6Ga_{10}O_{35}$ refined using the starting model from the International Centre for Diffraction Data (#ICDD) database entry 04-009-7303,[2] with space group *F*23. $Ca_{14}Zn_6Ga_{10}O_{35}$ is a cubic complex oxide with four distinct crystallographic sites for Ga. Among the three distinct crystallographic sites of Ca (Figures S2a–S2c), the 24*f* (Ca1) site forms a pentagonal bipyramid with Ca at 16*e* sites (Ca2 and Ca3) forming distorted octahedra. Ca1 edge-shares with Ca2 and Ca3 through common oxygen (O2 and O4) to form an octahedral cage around Ga at 4*b* sites (Ga3). Hence, Ga3 forms a regular octahedron isolated from tetrahedral Ga and Zn by Ca1, Ca2, and Ca3 (Figure S2b). Three Ca1 polyhedra are connected through the O3 oxygen atom to form regular and distorted tetrahedral voids for Ga at 4*a* sites (Ga1) and Ga at 16*e* sites (Ga4, occupied alongside Zn). Ga at 24*g* sites is tetrahedral (Ga2) and connected to Ga4 and Ca2 through the corner-shared oxygen atom O5 (Figure S2c). Large voids in the center are filled by a group of four vertex-linked tetrahedral units of Zn at 16*e* sites, which are further connected to tetrahedral Ga at 24*g* sites (Ga2) and Ca1 and Ca3 (Figure S2d).

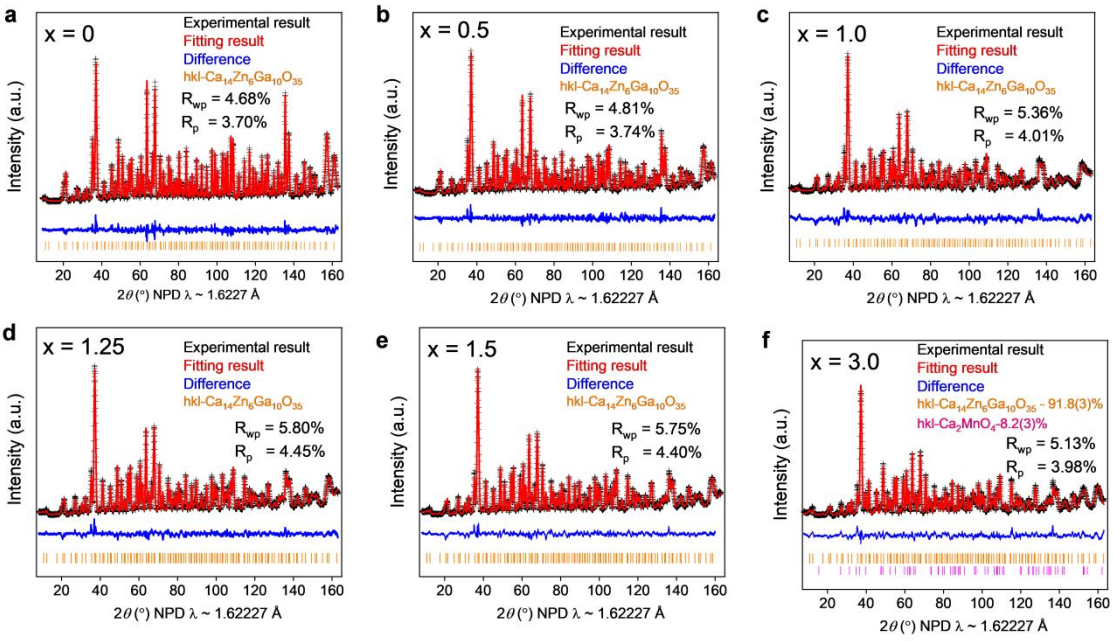


Figure S3. Neutron Rietveld refinement profiles (without the constraint of Mn content) for given wavelength λ = 1.62227 Å, for $Ca_{14}Zn_6Ga_{10-x}Mn_xO_{35}$ (x = 0, 0.3, 0.5, 1.0, 1.25, 1.5, and 3.0) samples (a) x = 0, (b) x = 0.5, (c) x = 1.0, (d) x = 1.25, (e) x = 1.5, and (f) x = 3.0. Black crosses and red solid lines are observed and calculated data, respectively. The blue line at the bottom is the difference between observed and calculated data. The orange vertical bars mark the position of Bragg reflections. For clarity, reflection markers hkl are referred to for the main phase as $Ca_{14}Zn_6Ga_{10}O_{35}$. The Ca_2MnO_4 impurity phase is found in x = 3.0 and reported as relative phase % with magenta reflection markers.

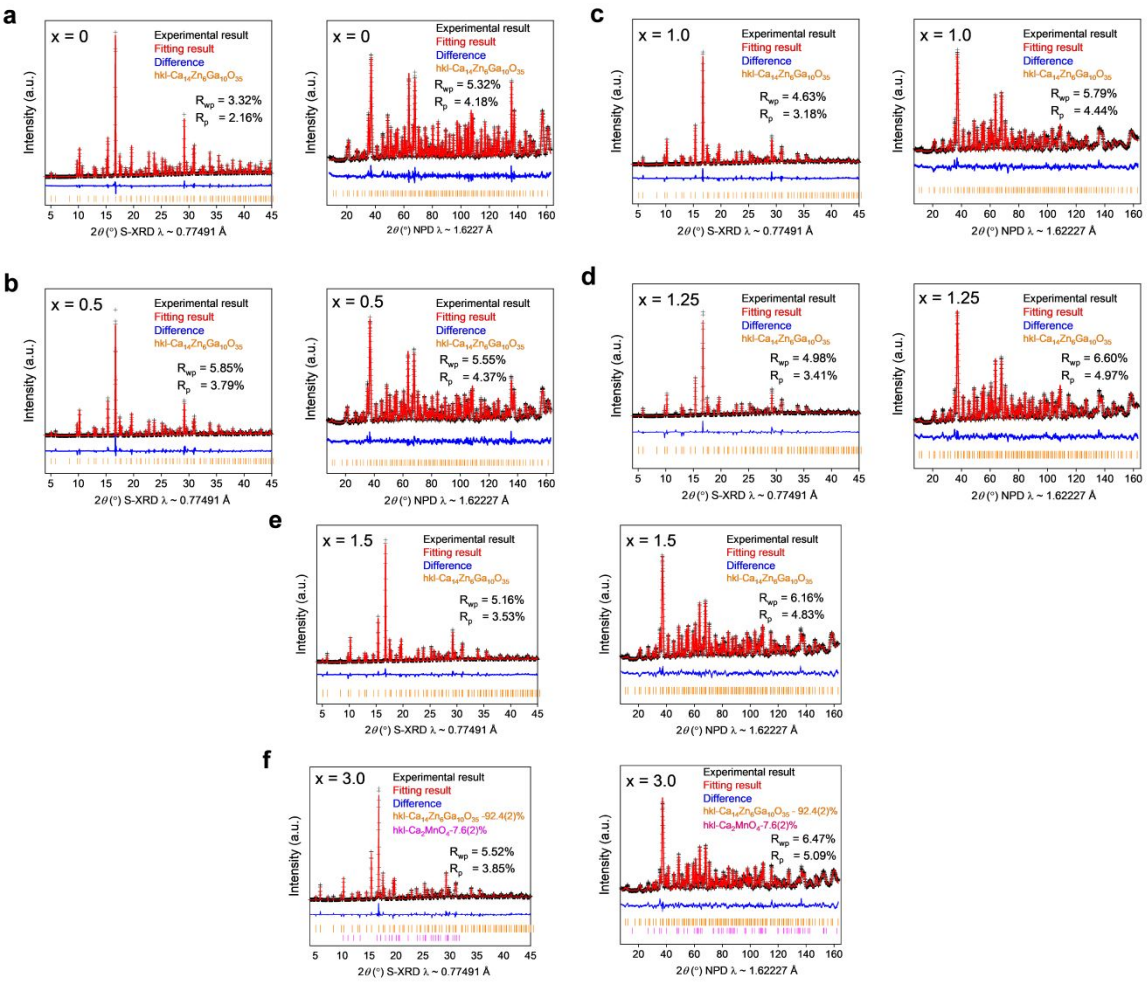


Figure S4. Joint Rietveld refinement profiles using S-XRD and NPD data (with the constraint of Mn content) for given wavelengths λ, for $Ca_{14}Zn_6Ga_{10-x}Mn_xO_{35}$ (x = 0, 0.3, 0.5, 1.0, 1.25, 1.5, and 3.0) samples (a), x = 0, (b) x = 0.5, (c) x = 1.0, (d) x = 1.25, (e) x = 1.5, and (f) x = 3.0. Black crosses and red solid lines are observed and calculated data, respectively. The blue line at the bottom is the difference between observed and calculated data. The orange vertical bars mark the position of Bragg reflections. For clarity, reflection markers hkl are referred to for the main phase as $Ca_{14}Zn_6Ga_{10}O_{35}$. The Ca_2MnO_4 impurity phase is found in x = 3.0 and reported as relative phase % with magenta reflection markers.

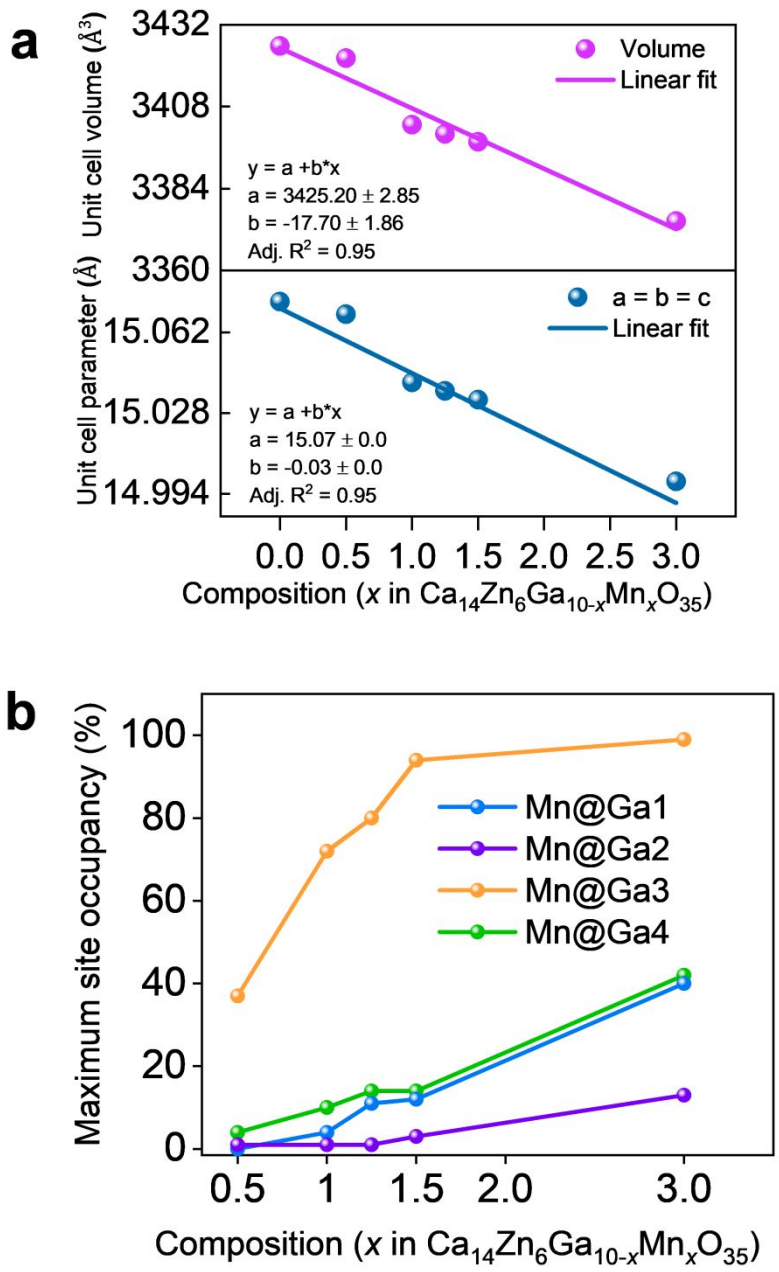


Figure S5. Joint Rietveld refinement results obtained from joint Rietveld refinement using S-XRD and NPD data (with constraint Mn content) of $Ca_{14}Zn_6Ga_{10-x}Mn_xO_{35}$ (x = 0, 0.3, 0.5, 1.0, 1.25, 1.5, and 3.0). (a) The lattice parameter, and volume along with linear fit. Estimated standard errors are smaller than the points. (b) Refined maximum site occupancy of Mn at each Ga site (lines through the points are a guide to the eye).

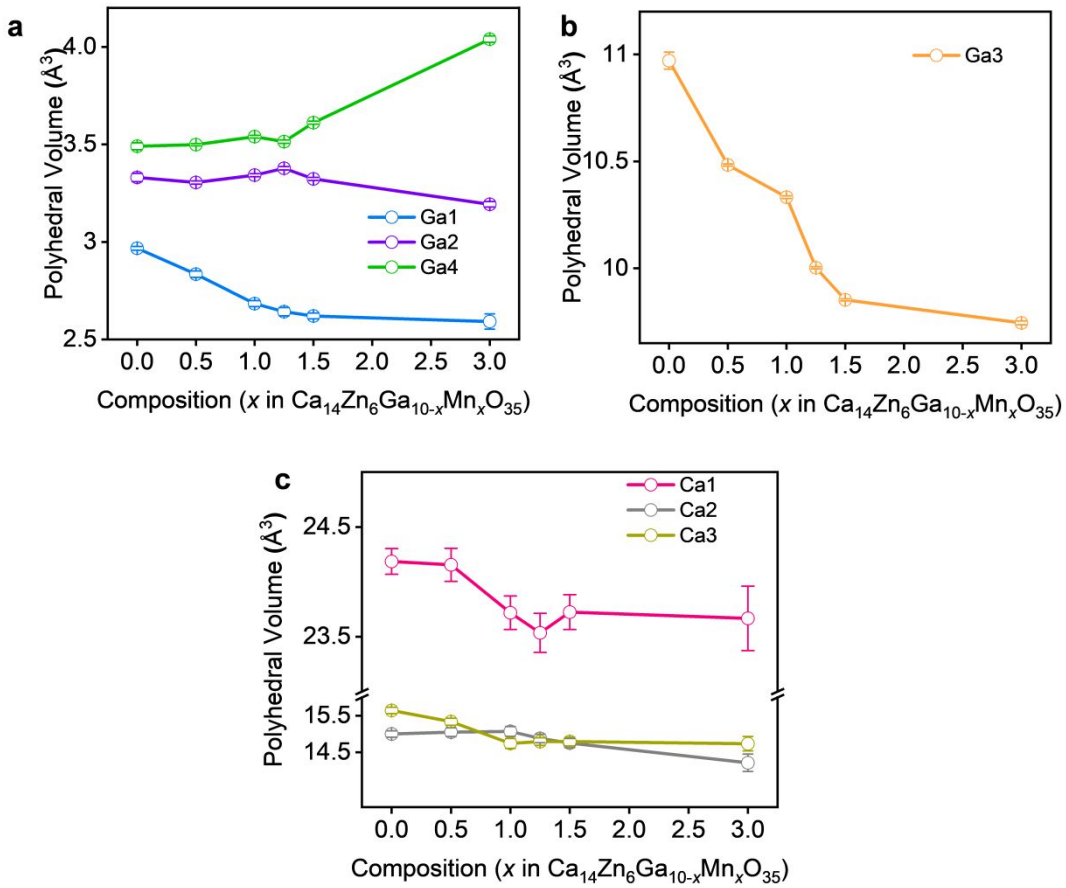


Figure S6. Volume of polyhedra in $Ca_{14}Zn_6Ga_{10-x}Mn_xO_{35}$ (x = 0, 0.5, 1.0, 1.25, 1.5, and 3.0) for sites (a) Ga1, Ga2, and Ga4 (b) Ga3, and (c) Ca1–Ca3 calculated from Rietveld refinement results using NPD data (without the constraint of Mn content). Lines through points are a guide to the eye.

The volume of polyhedra surrounding Ga sites calculated from the Rietveld refinement results of both approaches is shown in Figures S6 and S7, where a decrease in the volume of Ga1 and Ga3 site polyhedra is found with increasing Mn^{4+} content, consistent with the substitution of Mn for Ga. Concurrently, the volume of Ga4 site polyhedra increases (Figures S6a and S7a), a phenomenon that can be explained based on polyhedral distortion (Figure S8a), and the volume of Ca1, Ca2, and Ca3 site polyhedra (Figures S6c and S7c). No distortion is observed for Ga1 and Ga3 site polyhedra, in contrast to the relatively large distortion index for Ga4 and Ga2 sites, explaining the lower favorability of these sites for Mn. Structurally, the polyhedral edge of the Ga1 site is shared with three Ca1 polyhedral units and is further connected to Ga3 polyhedra through corner-sharing oxygen. Similarly, Ga3 polyhedra edge-share with Ca2 and Ca3 polyhedra. Hence, the concurrent occupation of Mn at Ga1 and Ga3 sites impacts the volume of Ca1 and Ca3 site polyhedra and increases the volume of Ga4 and Ca2 polyhedra.

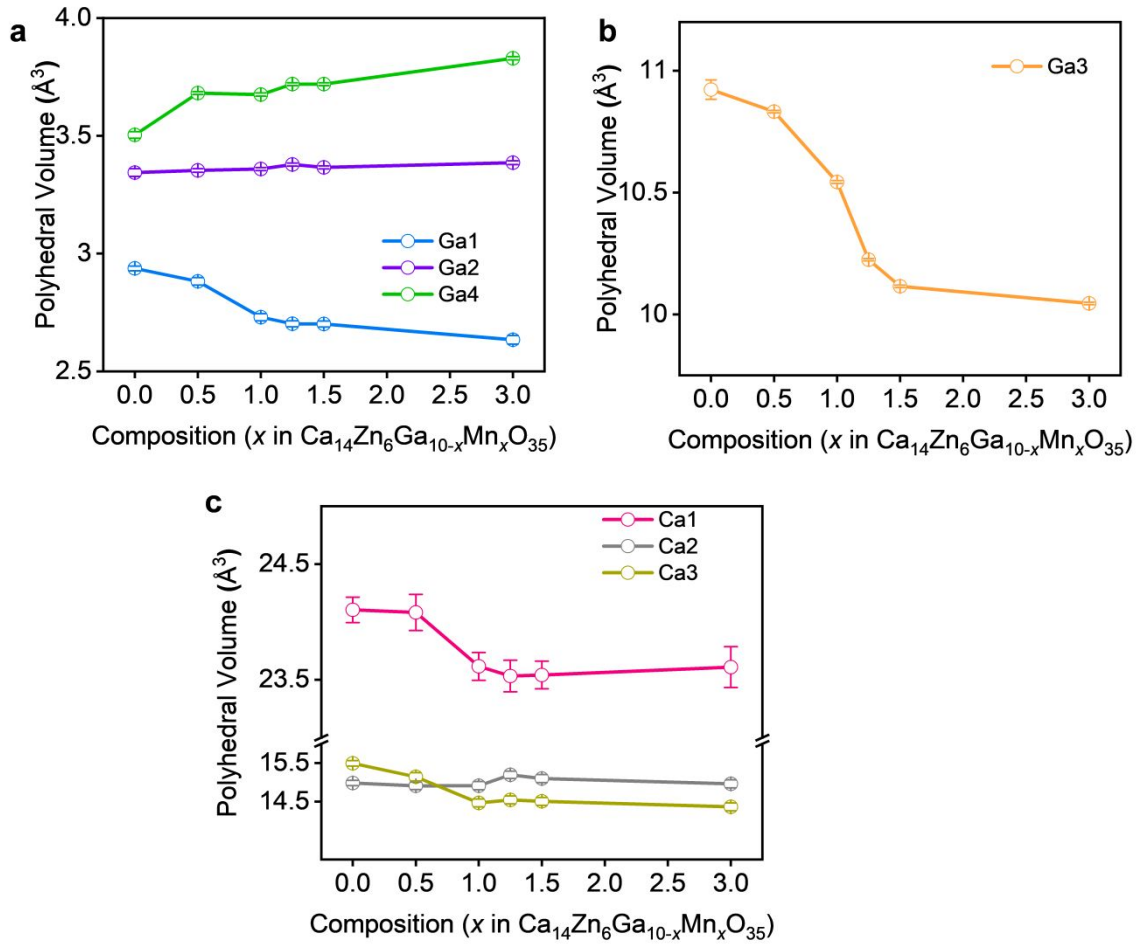


Figure S7. Volume of polyhedra in $Ca_{14}Zn_6Ga_{10-x}Mn_xO_{35}$ (x = 0, 0.5, 1.0, 1.25, 1.5, and 3.0) for sites (a) Ga1, Ga2, and Ga4 (b) Ga3, and (c) Ca1–Ca3 calculated from joint Rietveld refinement results (with the constraint of Mn content). Lines through points are a guide to the eye.

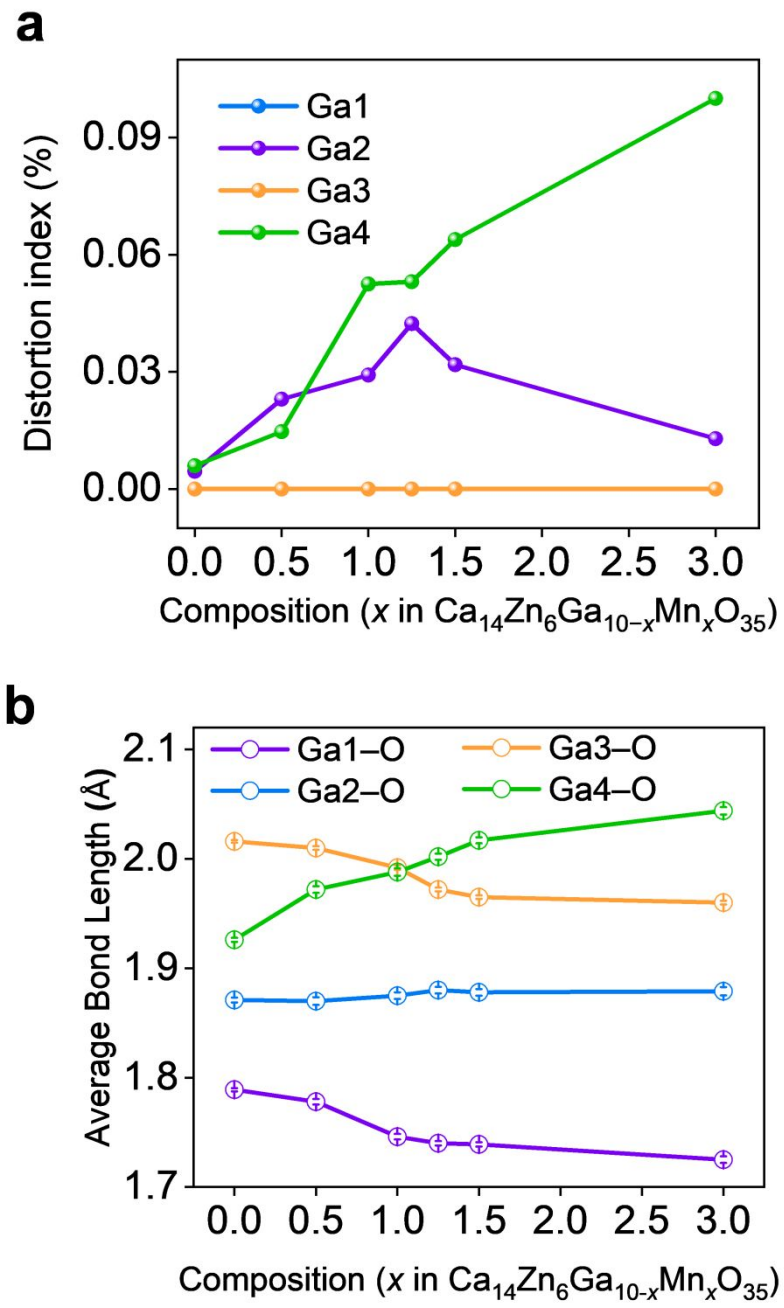


Figure S8. Joint Rietveld refinement results (with the constraint of Mn content) of $Ca_{14}Zn_6Ga_{10-x}Mn_xO_{35}$ (x = 0, 0.3, 0.5, 1.0, 1.25, 1.5, and 3.0). (a) Distortion index for Ga site polyhedra. The distortion index of M1 and M3 sites is zero. Lines through the points are a guide to the eye. (b) Ga–O average bond length for each Ga site. Lines through the points are a guide to the eye.

Short-range structure investigations (EPR and SQUID)

Electron paramagnetic resonance (EPR) spectroscopy and magnetometry measurements were made to investigate the state of Mn in the material series. At high symmetry, Mn^{4+} with spin S = 3/2 and the nuclear magnetic moment I = 5/2 is characterized by 6 EPR lines corresponding to hyperfine structure and 3 EPR lines corresponding to fine structure in superposition. Mn^{5+} with spin S = 1 does not produce an EPR signal in the X-band but contributes to the magnetic susceptibility in magnetometry. Given the lack of magnetic anisotropy, hyperfine interactions of Mn^{4+} are observable for weakly interacting (isolated) ions, whereas a single broad EPR line is found for Mn^{4+}–Mn^{4+} pair interactions in transition elements.[11-14] The RT EPR spectra of $Ca_{14}Zn_6Ga_{10-x}O_{35}$:$x$$Mn^{4+}$ (x = 0.3, 0.5, 1.0, 1.25, 1.5, and 3.0) samples are shown in Figure S9a. The hyperfine structure of Mn^{4+} (I = 5/2) is observed for lower Mn concentration x = 0.3 and 0.5 samples, whereas one broad EPR line (strong interactions) is observed for higher values of x. The Spin Hamiltonian parameters and the local symmetry of manganese ions were calculated using the EPR/NMR program.[15] Parameters were refined using the root-mean-square deviation method. Spin Hamiltonian (SH) calculations using Equations (S2) and (S3) including terms for Zeeman interactions (H_{Zeeman}), zero-field splitting (H_{ZFS}), hyperfine interactions (H_{HI}), and ion interactions (H_I), indicate the presence of two magnetically different Mn centers.

$$\boldsymbol{H = H_{Zeeman} + H_{ZFS} + H_{HI} + H_I}, \quad \text{(S2)}$$

$$\boldsymbol{H = \mu_B B \cdot g \cdot S + D\left(S_z^2 - \frac{1}{3}S(S+1)\right) + E\left(S_x^2 + S_y^2\right) + S \cdot A \cdot I + S^A \cdot D^{AB} \cdot S^B}, \quad \text{(S3)}$$

Where μ_B is the magnetic moment in Bohr magneton, B is the magnetic field, g is the spectroscopic splitting matrix including diagonal elements g_x, g_y, and g_z, S is the electron spin, D and E are axial and rhombic distortions of octahedra, respectively, A is the hyperfine interaction matrix including diagonal elements A_x, A_y, and A_z, I is the nuclear spin, and D^{AB} is the general interaction matrix between A and B ions with spins S_A and S_B, respectively.

In SH calculations, the magnetic moment of the electron (Bohr magnetons) is expressed as $\mu_B = e\hbar/2m_e$, where m_e, h, and e are the electron mass, Planck's constant, and electron charge, respectively. D^{AB} can be used to determine the strength of the interaction. Figures S9b and S9c show the least-squares fitting of SH parameters, and the results are summarized in Table S5. The SH parameters indicate the presence of two different paramagnetic centers, one from isolated Mn^{4+} (g = 1.9965) for $x \leq 0.5$ and one from manganese ion interactions. Both signals are assigned to manganese ions with high symmetry, in agreement with the Mn substitution obtained from Rietveld refinement. As x increases, the axial distortion of the nearest ion environment decreases, and the strength of the broad Mn ion interaction signal increases. This likely arises from the reduced distance between $Ga3O_6$ and $Ga1O_4$ units as x increases, promoting Ga3 and Ga1 spin interactions and increased D^{AB} (Figures S9d and S10).

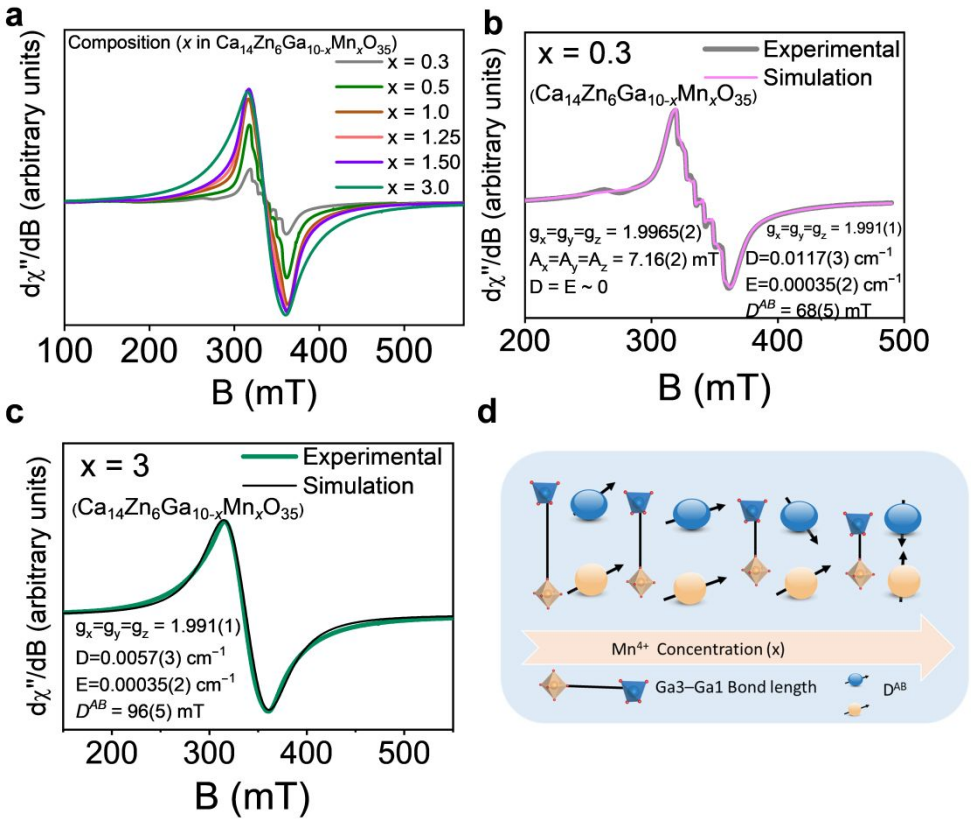


Figure S9. Short-range structure of $Ca_{14}Zn_6Ga_{10-x}Mn_xO_{35}$ (x = 0.3, 0.5, 1.0, 1.25, 1.5, and 3.0). (a), X-band EPR spectrum. (b), Least-squares fitting of SH parameters for x = 0.3 and c, x = 3.0. d, Schematic of the relationship between the Ga3–Ga1 distance (Ga3 is shown in yellow and Ga1 in blue, with correspondingly shaded polyhedra) and the general interaction matrix D^{AB} between A and B ions with spins S_A and S_B, respectively.

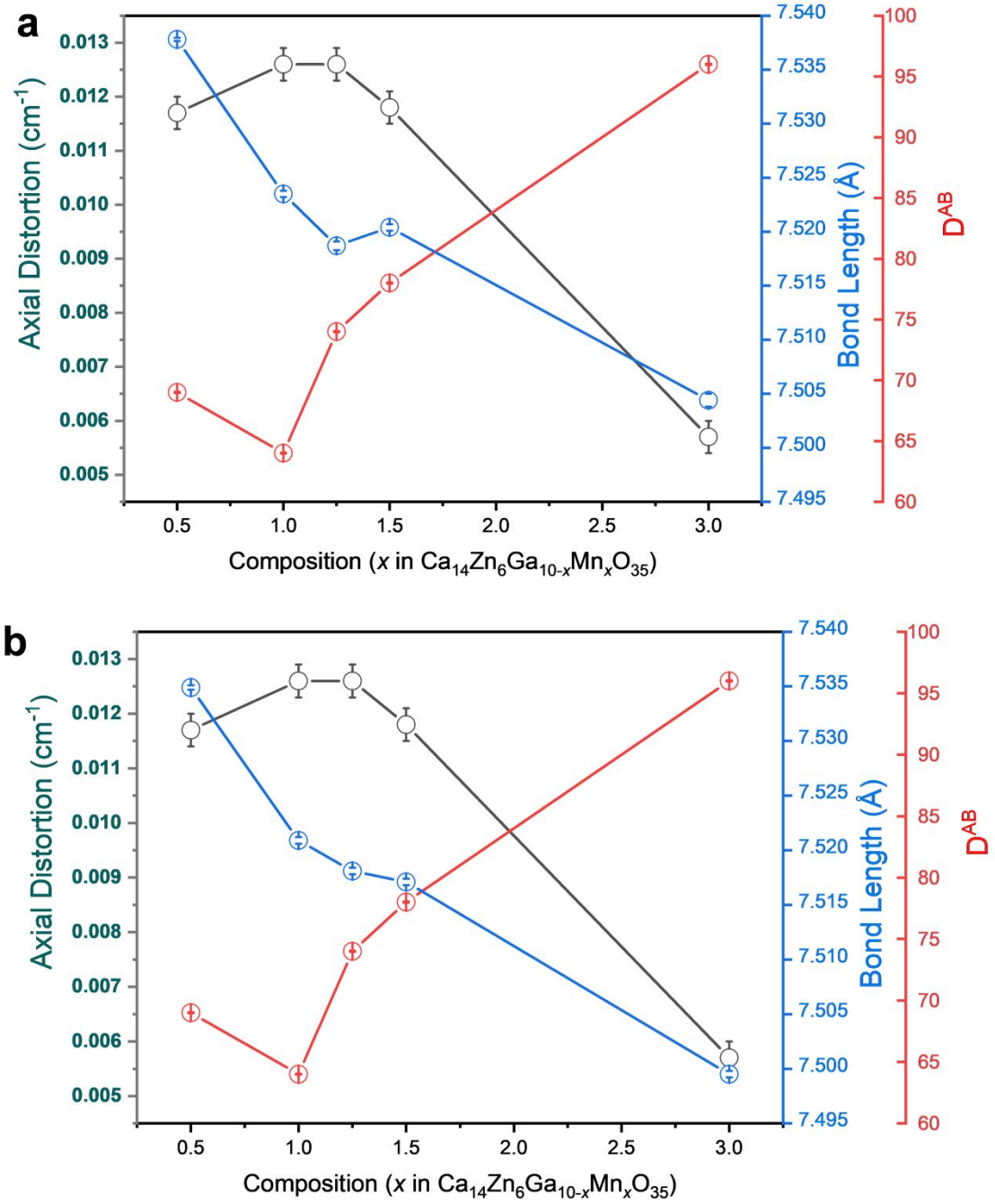


Figure S10. Axial distortion and D^{AB} (general interaction matrix between A and B ions with spins S_A and S_B, respectively), as well as the Ga3–Ga1 distance obtained from Rietveld refinement (a) using NPD data (without the constraint of Mn content) and (b) joint Rietveld refinements (with the constraint of Mn content) for the series $Ca_{14}Zn_6Ga_{10-x}Mn_xO_{35}$ (x = 0.3, 0.5, 1.0, 1.25, 1.5, and 3.0). Lines through points are a guide to the eye.

Temperature dependence magnetic susceptibility

The temperature dependence of magnetic susceptibility measured using EPR spectroscopy for x = 0.5–3.0 samples is shown in Figure S11, with the inverse magnetic susceptibility shown inset. For $x \geq 0.5$, magnetic susceptibility increases with temperature, indicating complex magnetic interactions between paramagnetic centers. Application of the Bleaney–Bowers equation for Mn ion interactions, as derived from Boltzmann's law, yields the total EPR intensity from the excited energy levels of the exchange-coupled Mn^{4+} and Mn^{5+} pair as per Equation (S4).[16]

$$\chi(T) = \frac{1\,P_1 exp(-J/kT) + P_2 exp(-3J/kT) + P_3 exp(-6J/kT) + P_4 exp(-10J/kT)}{T\,1 + 3exp\,(-J/kT) + 5exp\,(-3J/kT) + 7exp\,(-6J/kT) + 9exp\,(-10J/kT)}, \quad \text{(S4)}$$

where χ is the magnetic susceptibility (MS) with temperature T, k is Boltzmann's constant, P_i (i = 1, 2, 3, 4) are coefficients related to the transition probability within each multiplet, and J is the exchange interaction constant. A negative value of J indicates antiferromagnetic Mn^{4+}–Mn^{5+} interactions, which strengthen with increasing x. The Curie–Weiss temperature T_{CW} is determined from the inverse magnetic susceptibility ($1/\chi$, inset in Figure S11) using Equation (S5):

$$\frac{1}{\chi} = \frac{1}{C}(T - T_{CW}), \quad \text{(S5)}$$

where T is the temperature and C is a constant.

Notably, the nature and strength of Mn ion interactions are influenced by x. Ferromagnetic interactions (positive T_{CW}) dominate at lower Mn concentrations as high as x = 0.5, whereas antiferromagnetic interactions (negative T_{CW}) are not observed for x = 1.0 and $x \geq 1.25$. The changes in interactions and evolution of magnetic susceptibility with Mn concentration also indicate the presence of two types of magnetic centers. Single Mn^{4+} interacts ferromagnetically, whereas exchange-coupled Mn^{4+}–Mn^{5+} pairs interact

antiferromagnetically. Hence, isolated Mn^{4+} dominates at lower *x*, whereas Mn^{4+}–Mn^{5+} interactions dominate at higher *x*. Luminescence studies confirm the existence of two kinds of magnetic centers. Mn^{5+} is not observable in EPR measurements and can be investigated using SQUID magnetometry measurements in two modes: zero-field cooling (ZFC, Figure S11), and field cooling (FC, Figure S11) for selected magnetic fields up to 2 K. The temperature dependence of MS $\boldsymbol{\chi(T)}$ is described by the Curie–Weiss law (Equation S6):

$$\boldsymbol{\chi(T) = \chi_{dia} + \frac{C}{T - T_{CW}}}, \quad \text{(S6)}$$

where $\boldsymbol{\chi_{dia}}$ is the diamagnetic contribution, *C* is the Curie constant, *T* is temperature, and T_{CW} is the Curie–Weiss temperature. T_{CW} reveals the strength of Mn ion interactions. A weak antiferromagnetic interaction between Mn ions and a slight increase in these interactions is found with increasing *x* except in the *x* = 0.5 sample, as consistent with EPR measurements. The effective magnetic moment μ_{eff} is determined using Equation (S7):

$$\boldsymbol{\mu_{eff} = 2.827\sqrt{C}\mu_B}, \quad \text{(S7)}$$

Where μ_B is the magnetic moment in Bohr magneton, and C is the Curie constant. The effective magnetic moment decreases with increasing Mn concentration. For the lower concentration *x* = 0.3, $\mu_{eff} = 3.68\mu_B$, whereas for the higher concentration *x* = 3.0, $\mu_{eff} = 2.91\mu_B$. These magnetic moments are reasonably close to theoretically calculated moments for Mn^{4+} = $3.87\mu_B$ and Mn^{5+} = $2.83\mu_B$. The ratio of Mn^{4+} to Mn^{5+} can be calculated by considering extremely weak antiferromagnetic interactions and only two magnetic kinds of ions (Mn^{4+} and Mn^{5+}). Mn^{4+} constitutes 2/3 of all magnetic ions in the *x* = 0.5 sample but is only 1/3 of all magnetic ions for the *x* = 1.0 sample. The contribution

of isolated Mn^{4+} decreases with increasing *x,* which supports the Mn^{4+} to Mn^{5+} energy transfer proposed by our luminescence studies.

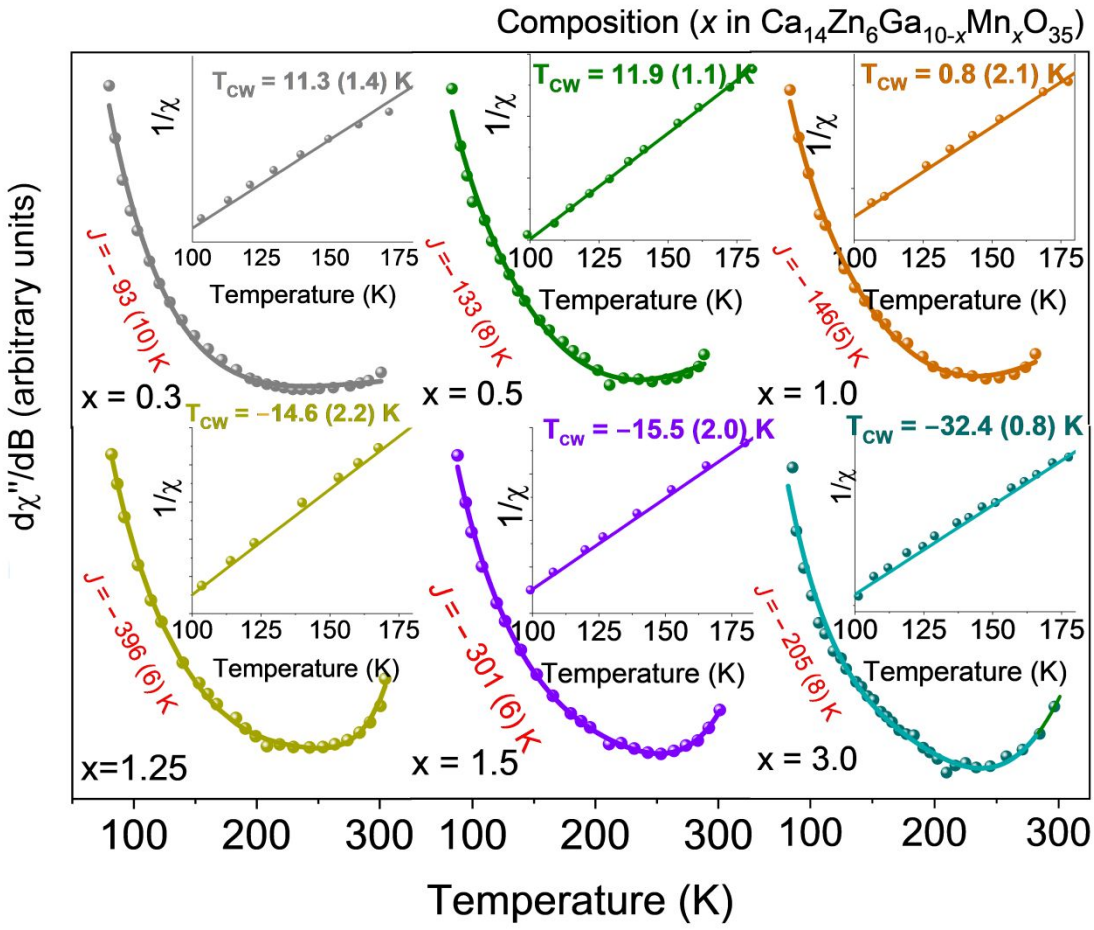


Figure S11. Dotted lines - temperature dependences of magnetic susceptibility calculated from EPR spectroscopy as the double integral of the EPR spectrum, solid lines - Bleaney–Bowers fitting. Inset in these is the inverse magnetic susceptibility versus temperature below 180 K, from which Curie-Weiss temperature, T_{CW}, was specified.

Different behaviors are observed in temperature-dependent FC SQUID MS (χ) measurements, where the dependence of the FC MS can be described by a combined Bleaney–Bowers and Curie–Weiss dependence as in Equation (S8):

$$\chi = \frac{C_1}{T} \cdot \frac{1}{1 + (1/3)exp\,(-2J/kT)}(1-\rho) + \frac{C}{T - T_{CW}}\rho, \qquad \text{(S8)}$$

where C and C_1 are constants, ρ is the contribution of the Curie–Weiss term, and other terms are per Equation (S4). Although the MS dependence shows typical ion–pair interactions, structural characterization studies exclude the formation of the Mn^{4+}–Mn^{4+} pair. Further, Mn^{5+}–Mn^{5+} pair interactions cannot be observed in X-band EPR measurements, whereas Mn^{4+}–Mn^{5+} can form a paramagnetic system that can be observed using EPR as a broad line centered at g = 2, as we find. Therefore, our magnetic susceptibility studies confirm the occurrence of Mn^{4+}–Mn^{5+} interactions and energy transfer between these ions. In relation to PL, the observation of red (650–750 nm) and NIR emissions (1100–1250 nm) in $Ca_{14}Zn_6Ga_{10}O_{35}$ probably arise from the occupation of Mn at Ga3 and Ga1 sites as Mn^{4+} and Mn^{5+}, respectively.

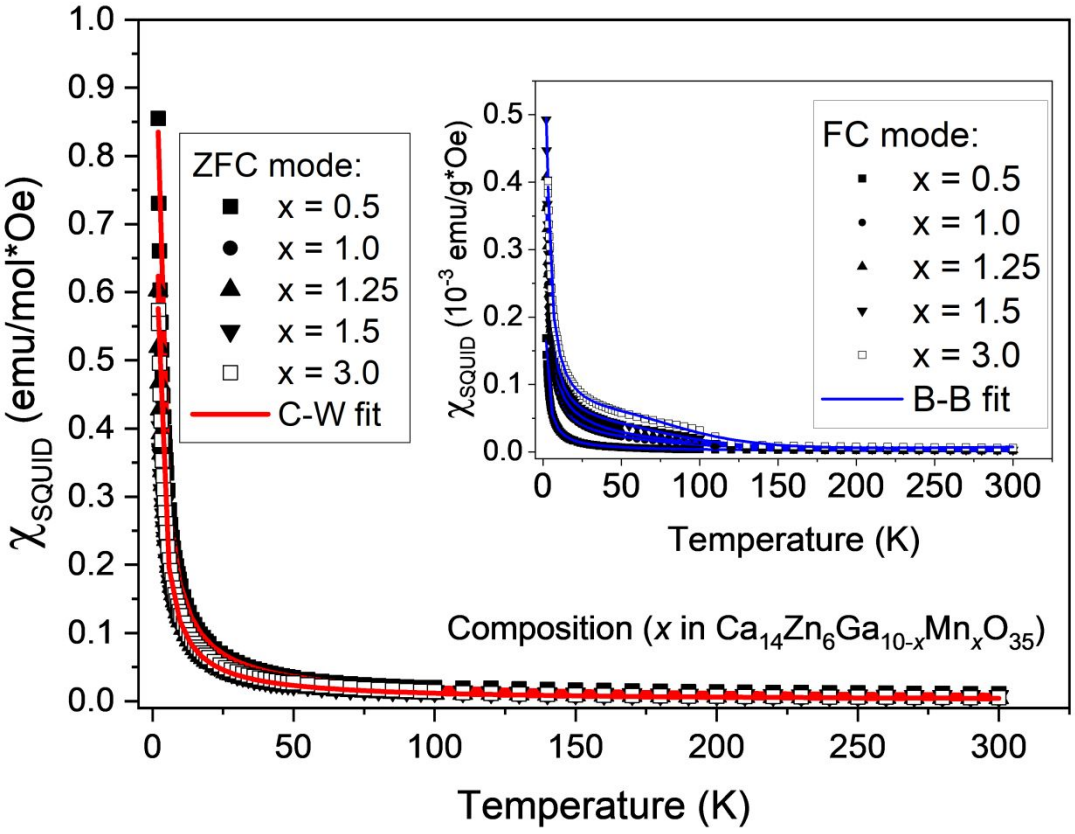


Figure S12. Magnetic susceptibility of $Ca_{14}Zn_6Ga_{10-x}Mn_xO_{35}$ (x = 0.3, 0.5, 1.0, 1.25, 1.5, and 3.0) in zero–field cooling (ZFC) and field cooling (FC) mode. Solid squares, solid circles, solid upward and downward triangles, and hollow squares are experimental points and continuous red and blue lines are fits of the standard Curie–Weiss and Bleaney–Bowers equations, respectively.

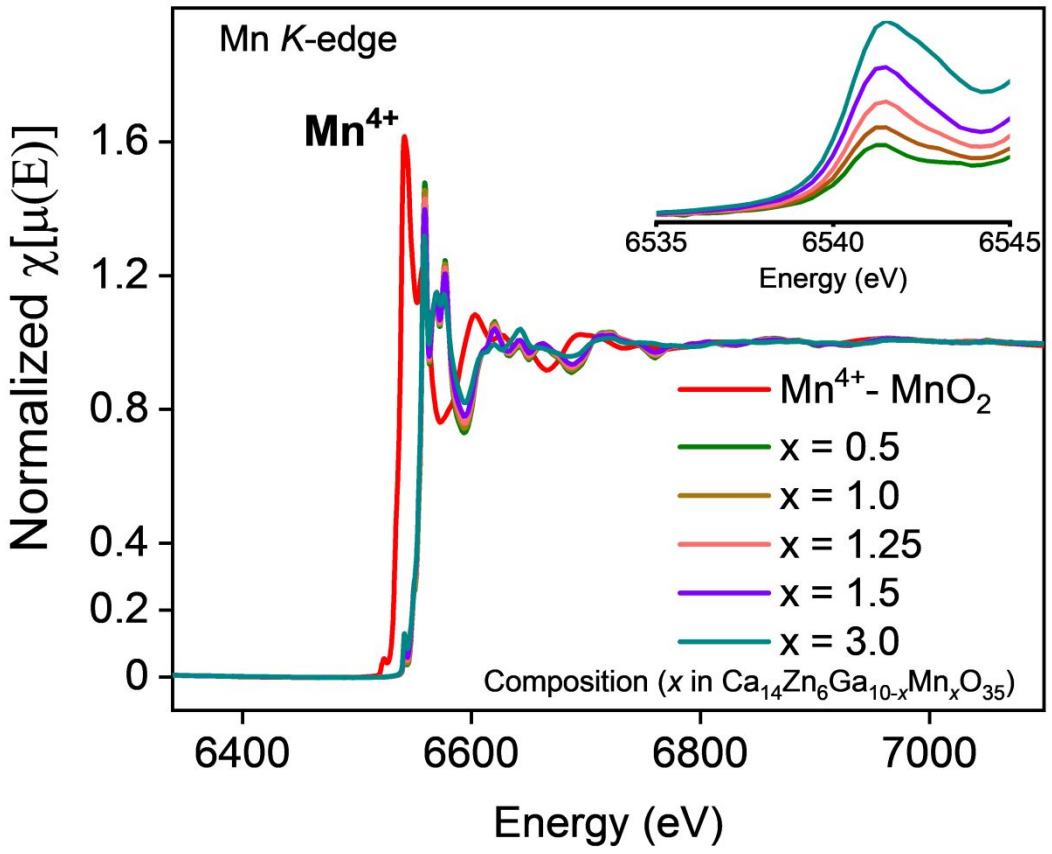


Figure S13. Normalized Mn *K*-edge X-ray absorption near-edge structure spectra of $Ca_{14}Zn_6Ga_{10-x}Mn_xO_{35}$ (x = 0.5, 1.0, 1.25, 1.5, and 3.0). The inset shows detail at near-edge features around 6535–6545 eV.

A strong pre-edge at 6541 eV and main edge at 6554 eV are observed in Mn *K*-edge X-ray absorption near-edge structure measurements (Figure S13). The intensity of the pre-edge at 6541 eV increases with increasing Mn concentration (inset in Figure S11), and the position of the main edge deviates from that for the +4 valence in comparison with the MnO_2 standard. The overlap between spectra of the MnO_2 standard and samples is noticeable, where the pre-edge corresponds to a tetrahedral environment.[17-18] Taken together with luminescence studies, we find $Ca_{14}Zn_6Ga_{10-x}O_{35}$:$x$$Mn^{4+}$ (x = 0.3, 0.5, 1.0, 1.25, 1.5, and 3.0) to contain Mn in both +4 and +5 valence states.

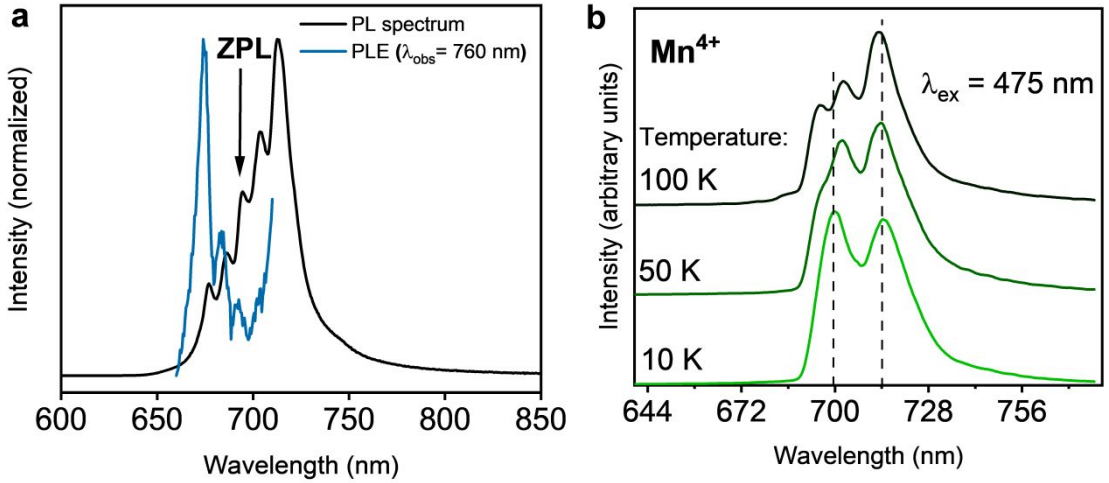


Figure S14. (a) Comparison of PL and PLE spectra in the range 660 – 710 nm (emission wavelength λ_{em} = 760 nm), with the zero phonon line (ZPL), (b) Mn^{4+} emission spectra at the excitation wavelength λ_{ex} = 475 nm in the range of 10–100 K. Spectra are offset in y for clarity. PL spectra exhibit unusual behavior at low temperatures, i.e., below 100 K, where the ZPL shifts slightly and vanishes, likely merging with the adjacent phonon line which gains intensity Dashed vertical lines are a guide to the eye.

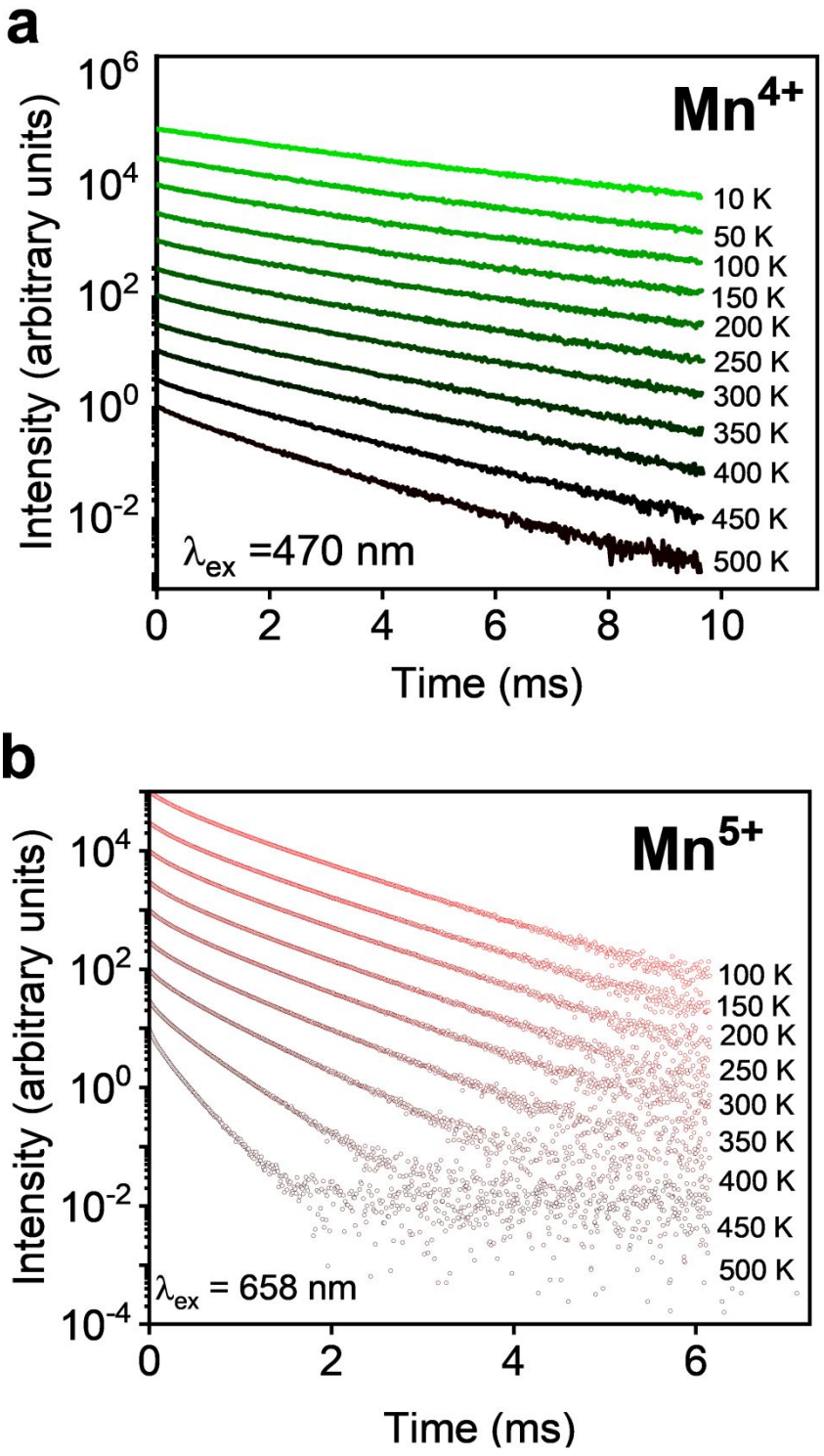


Figure S15. Temperature dependence decay profile of (a) x = 0.5 (Mn^{4+}) and (b) x = 1 (Mn^{5+}) luminescence intensity at excitation wavelengths (λ_{ex}) of 470 and 658 nm, respectively.

Pressure-Dependent Photoluminescence

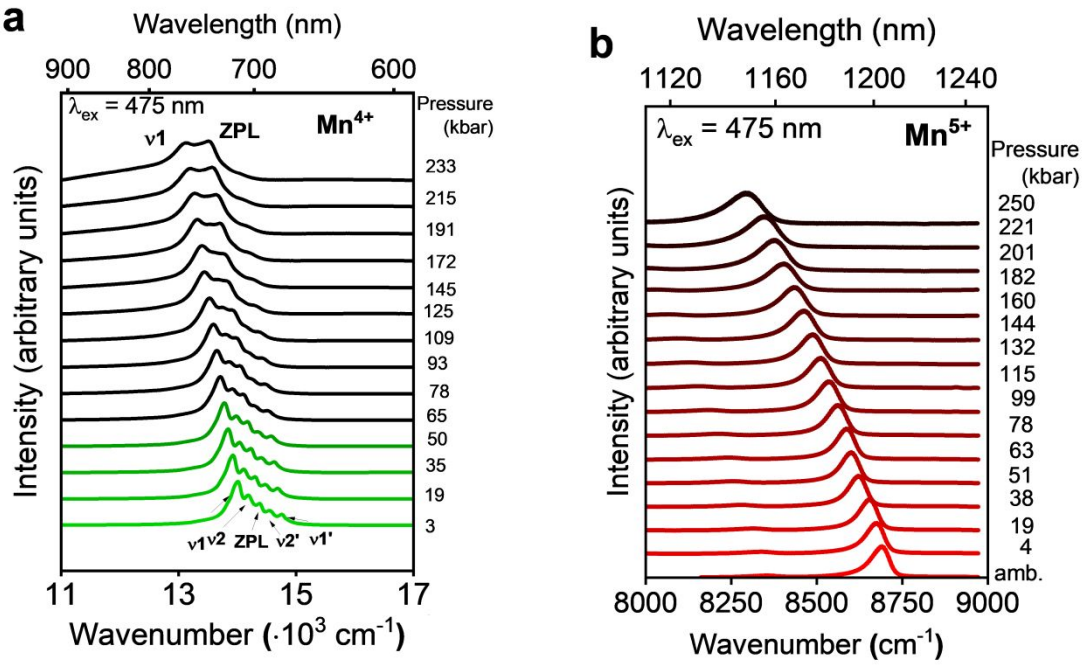


Figure S16. (a) Normalized room-temperature emission spectra at different pressure, with a 475 nm excitation λ_{ex} for Mn^{4+} ($x = 0.5$). The zero phonon line (ZPL) and visible phonon modes $\nu1$ and $\nu2$ in Stokes phonon sidebands and $\nu2'$ and $\nu1'$ in anti-Stokes phonon sidebands are labeled, (b) Normalized RT emission spectra at different pressure values offset in y for clarity, using an excitation wavelength (λ_{ex}) of 475 nm for $x = 1$ (Mn^{5+}).

The RT pressure-dependent luminescence spectra of Mn^{4+} and Mn^{5+} measured up to 250 kbar pressure upon 475 nm excitation are shown in Figures S14a and S14b. As pressure increases, a linear shift toward lower energies is observed for Mn^{4+} and Mn^{5+} emissions (Table S7). Additionally, the emission spectrum of Mn^{4+} is significantly broadened with increasing pressure, and fine spectral features are no longer well resolved. Nonetheless, the ZPL line begins to dominate the $\nu1$ line, which is most intense at ambient pressure. This effect can be related to the induction of static distortion around the Mn^{4+} site, which increases the probabilities of ZPL emission.

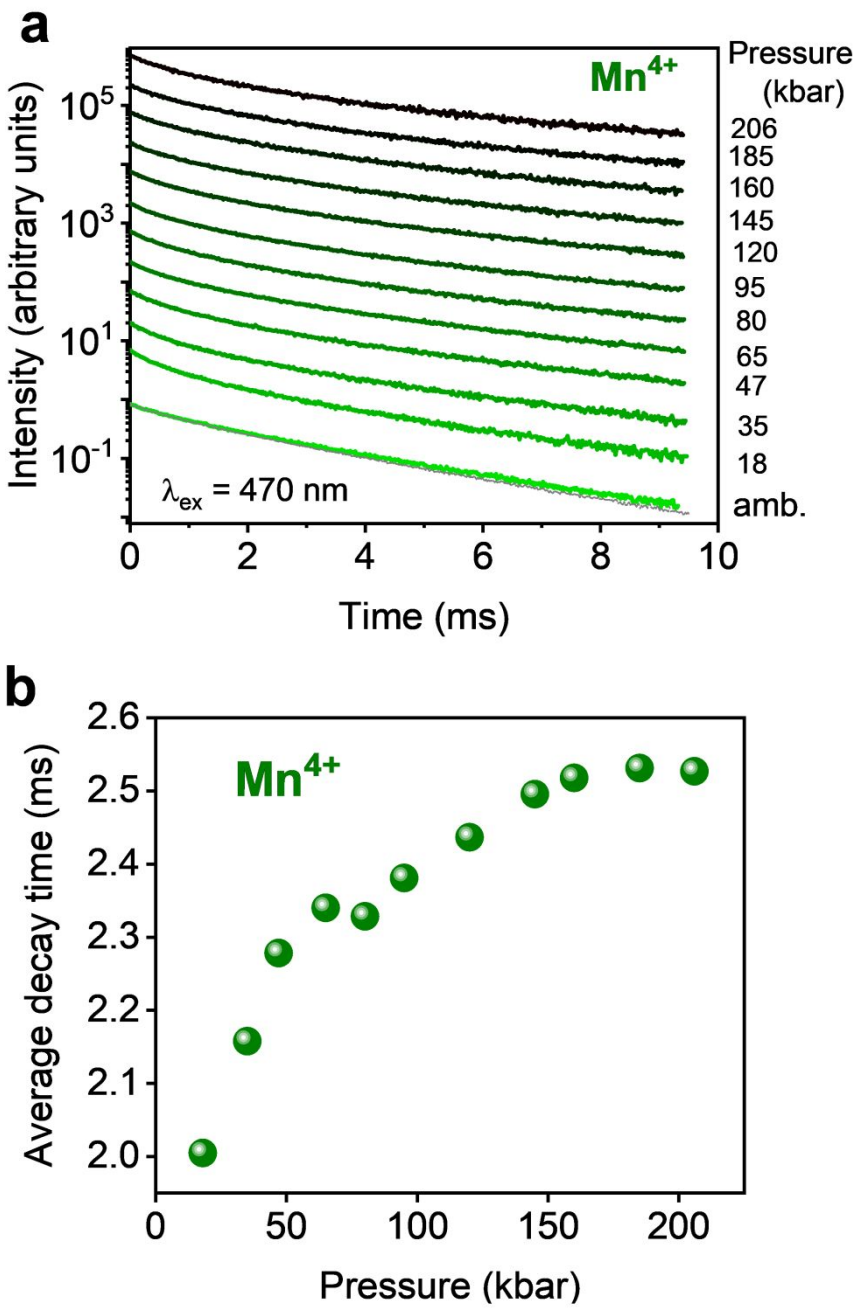


Figure S17. (a) Pressure-dependent decay of Mn^{4+} luminescence intensity ($x = 0.5$) at an excitation wavelength λ_{ex} of 470 nm. The grey line is the decay after the release of pressure. (b) Calculated decay times of Mn^{4+} luminescence intensity ($x = 0.5$) for different pressures. Errors are smaller than the points.

The pressure-dependent decay of the Mn^{4+} emission intensity under 470 nm excitation is non-exponential (Figure S15a). The average decay time is calculated using Equation (1) and shown in Figure 15b. The decay time increases with increasing pressure up to 150 kbars and then reaches a plateau. The initial increase in decay time is due to a

pressure-induced increase in crystal field strength, which increases the energy difference between $^4T_2$ and ^2E levels. In effect, the mixing between ^2E and $^4T_2$ states due to spin–orbital interaction decreases (equivalent to an increase of the Δ parameter), reducing the probability of the spin-forbidden $^2E \rightarrow {}^4A_2$ transition.[19] The flattening of the luminescence intensity decay at high pressure is caused by the pressure-induced breaking of the parity selection rule by inducing static distortions of the Mn^{4+} site or additional non-radiative de-excitation channels. This finding is consistent with the increased ZPL intensity with pressure (Figure S14a).

Table S1. The lattice parameter, volume, phase composition, and figures of merit for Rietveld refinements using NPD data performed without the constraint of Mn content of $Ca_{14}Zn_6Ga_{10-x}Mn_xO_{35}$ (x = 0, 0.5, 1.0, 1.25, 1.5, and 3.0).

x	**0**	**0.5**	**1**	**1.25**	**1.5**	**3**
$a = b = c$ (Å)	15.0772(2)	15.0750(3)	15.0477(5)	15.0416(5)	15.0383(7)	15.0087(10)
V (Å^3)	3427.4(1)	3425.9(2)	3407.3(3)	3403.2(3)	3400.9(4)	3380.9(7)
Weighted R-profile (R_{wp}) and R-profile (R_p) factors for the NPD data histogram						
R_{wp} (%)	4.68	4.81	5.36	5.80	5.75	5.13
R_p (%)	3.70	3.74	4.01	4.45	4.40	3.98
Phase Fractions						
Main Phase (%)	100	100	100	100	100	91.8(3)
Ca_2MnO_4 (%)						8.2(3)

Table S2. Atomic parameters obtained from Rietveld refinement using NPD data performed without any constraint of Mn content of $Ca_{14}Zn_6Ga_{10-x}Mn_xO_{35}$ (x = 0, 0.5, 1.0, 1.25,1.5, and 3.0).

x = 0				$Ca_{14}Zn_6Ga_{10}O_{35}$			
Site	x	y	z	**Wyckoff Site**	**Occ**	**Beq (Å²)**	**Atoms**
Ca1	0.2127(2)	0	0	24*f*	1	0.72(6)	24
Ca2	0.6126(3)	0.6126(3)	0.6126(3)	16*e*	1	0.62(9)	16
Ca3	0.3886(3)	0.3886(3)	0.3886(3)	16*e*	1	0.77(9)	16
Zn1	0.1733(1)	0.1733(1)	0.1733(1)	16*e*	1	0.22(5)	16
Ga1	0	0	0	4*a*	1	0.52(11)	4
Ga2	−0.0012(4)	0.2500	0.2500	24*g*	1	0.60(3)	24
Ga3	0.5000	0.5000	0.5000	4*b*	1	0.45(11)	4
Ga4	0.8566(1)	0.8566(1)	0.8566(1)	16*e*	0.5	1.13(7)	8
Zn4	0.8566(1)	0.8566(1)	0.8566(1)	16*e*	0.5	1.13(7)	8
O1	0.2500	0.2500	0.2500	4*c*	1	0.41(10)	4
O2	0.3661(2)	0	0	24*f*	1	0.47(4)	24
O3	−0.0687(2)	−0.0687(2)	−0.0687(2)	16*e*	1	1.69(8)	16
O4	0.0694(3)	0.2574(2)	0.3521(3)	48*h*	1	0.87(8)	48
O5	0.1473(3)	0.2529(2)	0.5699(3)	48*h*	1	0.83(7)	48

x = 0.5				$Ca_{14}Zn_6Ga_{9.0(2)}Mn_{1.0(2)}O_{35}$			
Site	x	y	z	**Wyckoff Site**	**Occ**	**Beq (Å²)**	**Atoms**
Ca1	0.2122(3)	0	0	24*f*	1	0.94(9)	24
Ca2	0.6133(4)	0.6133(4)	0.6133(4)	16*e*	1	1.10(16)	16
Ca3	0.3874(3)	0.3874(3)	0.3874(3)	16*e*	1	0.48(12)	16
Zn1	0.1741(2)	0.1741(2)	0.1741(2)	16*e*	1	0.40(8)	16
Ga1	0	0	0	4*a*	1.00(2)	0.7(2)	4.00(8)
Ga2	−0.0007(6)	0.2500	0.2500	24*g*	0.951(6)	0.40(5)	22.824(144)
Mn2	−0.0007(6)	0.2500	0.2500	24*g*	0.049(6)	0.40(5)	1.176(144)
Ga3	0.5000	0.5000	0.5000	4*b*	0.572(19)	0.6(6)	2.288(76)
Mn3	0.5000	0.5000	0.5000	4*b*	0.428(19)	0.6(6)	1.712(76)
Ga4	0.8558(2)	0.8558(2)	0.8558(2)	16*e*	0.422(10)	1.09(13)	6.752(160)
Mn4	0.8558(2)	0.8558(2)	0.8558(2)	16*e*	0.078(10)	1.09(13)	1.248(160)
Zn4	0.8558(2)	0.8558(2)	0.8558(2)	16*e*	0.5	1.09(13)	8
O1	0.2500	0.2500	0.2500	4*c*	1	0.65(15)	4
O2	0.3676(2)	0	0	24*f*	1	0.47(5)	24
O3	−0.0680(3)	−0.0680(3)	−0.0680(3)	16*e*	1	1.99(11)	16
O4	0.0690(4)	0.2561(3)	0.3527(4)	48*h*	1	1.10(12)	48
O5	0.1475(4)	0.2533(3)	0.5691(4)	48*h*	1	1.17(12)	48

$x = 1.0$				$Ca_{14}Zn_6Ga_{8.7(3)}Mn_{1.3(3)}O_{35}$			
Site	***x***	***y***	***z***	**Wyckoff Site**	**Occ**	**Beq (Å²)**	**Atoms**
Ca1	0.2140(4)	0	0	24*f*	1	1.56(13)	24
Ca2	0.6180(5)	0.6180(5)	0.6180(5)	16*e*	1	1.5(2)	16
Ca3	0.3889(4)	0.3889(4)	0.3889(4)	16*e*	1	0.19(15)	16
Zn1	0.1754(2)	0.1754(2)	0.1754(2)	16*e*	1	0.21(12)	16
Ga1	0	0	0	4*a*	0.98(2)	1.8(3)	3.92(8)
Mn1	0	0	0	4*a*	0.02(2)	1.8(3)	0.08(8)
Ga2	0.0029(5)	0.2500	0.2500	24*g*	0.962(8)	0.64(8)	23.088(192)
Mn2	0.0029(5)	0.2500	0.2500	24*g*	0.038(8)	0.64(8)	0.912(192)
Ga3	0.5000	0.5000	0.5000	4*b*	0.13(6)	20(9)	0.52(24)
Mn3	0.5000	0.5000	0.5000	4*b*	0.87(6)	20(9)	3.48(24)
Ga4	0.8509(4)	0.8509(4)	0.8509(4)	16*e*	0.463(16)	4.3(3)	7.408(256)
Mn4	0.8509(4)	0.8509(4)	0.8509(4)	16*e*	0.037(16)	4.3(3)	0.592(256)
Zn4	0.8509(4)	0.8509(4)	0.8509(4)	16*e*	0.5	4.3(3)	8
O1	0.2500	0.2500	0.2500	4*c*	1	1.1(2)	4
O2	0.3680(3)	0	0	24*f*	1	0.47(7)	24
O3	−0.0670(3)	−0.0670(3)	−0.0670(3)	16*e*	1	2.03(15)	16
O4	0.0702(4)	0.2523(5)	0.3603(4)	48*h*	1	1.80(12)	48
O5	0.1513(3)	0.2541(3)	0.5683(3)	48*h*	1	0.40(8)	48

$x = 1.25$				$Ca_{14}Zn_6Ga_{8.5(2)}Mn_{1.5(2)}O_{35}$			
Site	***x***	***y***	***z***	**Wyckoff Site**	**Occ**	**Beq (Å²)**	**Atoms**
Ca1	0.2132(3)	0	0	24*f*	1	1.37(10)	24
Ca2	0.6170(4)	0.6170(4)	0.6170(4)	16*e*	1	1.55(18)	16
Ca3	0.3886(3)	0.3886(3)	0.3886(3)	16*e*	1	0.39(13)	16
Zn1	0.1746(2)	0.1746(2)	0.1746(2)	16*e*	1	0.26(10)	16
Ga1	0	0	0	4*a*	0.932(19)	1.5(2)	3.728(76)
Mn1	0	0	0	4*a*	0.068(19)	1.5(2)	0.272(76)
Ga2	0.0028(4)	0.2500	0.2500	24*g*	0.951(7)	0.78(7)	22.824(168)
Mn2	0.0028(4)	0.2500	0.2500	24*g*	0.049(7)	0.78(7)	1.176(168)
Ga3	0.5000	0.5000	0.5000	4*b*	0.06(3)	7.9(18)	0.24(12)
Mn3	0.5000	0.5000	0.5000	4*b*	0.94(3)	7.9(18)	3.76(12)
Ga4	0.8515(3)	0.8515(3)	0.8515(3)	16*e*	0.449(13)	3.7(3)	7.184(52)
Mn4	0.8515(3)	0.8515(3)	0.8515(3)	16*e*	0.051(13)	3.7(3)	0.816(52)
Zn4	0.8515(3)	0.8515(3)	0.8515(3)	16*e*	0.5	3.7(3)	8
O1	0.2500	0.2500	0.2500	4*c*	1	0.96(17)	4
O2	0.3697(2)	0	0	24*f*	1	0.61(6)	24
O3	−0.0669(3)	−0.0669(3)	−0.0669(3)	16*e*	1	2.16(13)	16
O4	0.0684(4)	0.2529(4)	0.3585(4)	48*h*	1	2.02(12)	48
O5	0.1499(2)	0.2534(3)	0.5686(3)	48*h*	1	0.56(7)	48

x = 1.5			$Ca_{14}Zn_6Ga_{8.5(3)}Mn_{1.5(3)}O_{35}$				
Site	x	y	z	**Wyckoff Site**	**Occ**	**Beq (Å²)**	**Atoms**
Ca1	0.2136(3)	0	0	24*f*	1	1.00(9)	24
Ca2	0.6163(4)	0.6163(4)	0.6163(4)	16*e*	1	1.65(19)	16
Ca3	0.3884(4)	0.3884(4)	0.3884(4)	16*e*	1	0.58(14)	16
Zn1	0.17449(16)	0.17449(16)	0.17449(16)	16*e*	1	0.06(10)	16
Ga1	0	0	0	4*a*	0.872(19)	1.3(3)	3.488(76)
Mn1	0	0	0	4*a*	0.128(19)	1.3(3)	0.512(76)
Ga2	0.0037(4)	0.2500	0.2500	24*g*	0.947(7)	0.84(7)	22.728(168)
Mn2	0.0037(4)	0.2500	0.2500	24*g*	0.053(7)	0.84(7)	1.272(168)
Ga3	0.5000	0.5000	0.5000	4*b*	0.05(3)	3.3(9)	0.2(12)
Mn3	0.5000	0.5000	0.5000	4*b*	0.95(3)	3.3(9)	3.8(12)
Ga4	0.8498(4)	0.8498(4)	0.8498(4)	16*e*	0.466(14)	5.0(3)	7.456(224)
Mn4	0.8498(4)	0.8498(4)	0.8498(4)	16*e*	0.034(14)	5.0(3)	0.476(224)
Zn4	0.8498(4)	0.8498(4)	0.8498(4)	16*e*	0.5	5.0(3)	8
O1	0.2500	0.2500	0.2500	4*c*	1	0.82(16)	4
O2	0.3704(2)	0	0	24*f*	1	0.90(6)	24
O3	−0.0662(3)	−0.0662(3)	−0.0662(3)	16*e*	1	2.31(14)	16
O4	0.0685(4)	0.2536(4)	0.3577(4)	48*h*	1	1.91(13)	48
O5	0.1493(3)	0.2529(3)	0.5678(3)	48*h*	1	0.79(9)	48

x = 3.0			$Ca_{14}Zn_6Ga_{7.8(6)}Mn_{2.2(4)}O_{35}$				
Site	x	y	z	**Wyckoff Site**	**Occ**	**Beq (Å²)**	**Atoms**
Ca1	0.2159(5)	0	0	24*f*	1	0.76(13)	24
Ca2	0.6145(7)	0.6145(7)	0.6145(7)	16*e*	1	1.0(3)	16
Ca3	0.3867(7)	0.3867(7)	0.3867(7)	16*e*	1	0.9(3)	16
Zn1	0.1761(3)	0.1761(3)	0.1761(3)	16*e*	1	0.15(16)	16
Ga1	0	0	0	4*a*	0.50(4)	2.0(18)	2.00(8)
Mn1	0	0	0	4*a*	0.50(4)	2.0(18)	2.00(8)
Ga2	0.0025(9)	0.2500	0.2500	24*g*	0.887(13)	0.77(13)	21.288(312)
Mn2	0.0025(9)	0.2500	0.2500	24*g*	0.113(13)	0.77(13)	2.712(312)
Mn3	0.5000	0.5000	0.5000	4*b*	1.00(6)	7(2)	4.00(24)
Ga4	0.8428(6)	0.8428(6)	0.8428(6)	16*e*	0.50(3)	6.4(8)	8.00(48)
Zn4	0.8428(6)	0.8428(6)	0.8428(6)	16*e*	0.5	6.4(8)	8
O1	0.2500	0.2500	0.2500	4*c*	1	1.7(3)	4
O2	0.3707(4)	0	0	24*f*	1	0.86(10)	24
O3	−0.0660(8)	−0.0660(8)	−0.0660(8)	16*e*	1	4.3(3)	16
O4	0.0684(4)	0.2519(6)	0.3490(5)	48*h*	1	0.65(10)	48
O5	0.1416(8)	0.2503(10)	0.5636(9)	48*h*	1	4.0(3)	48
$Ca_2Mn_{1.00(24)}O_4$							
O1	0	0	0.1599(10)	4*e*	1	0.6(2)	4
Ca1	0	0	0.3569(11)	4*e*	1	0.4(3)	4
O2	0	0.5	0	4*c*	1	2.5(3)	4
Mn1	0	0	0	2*a*	1.00(12)	1.9(9)	2.00(24)

Table S3. Lattice parameters, volume, phase composition, and figures of merit obtained from joint Rietveld refinements performed with the constraint of Mn content of $Ca_{14}Zn_6Ga_{10-x}Mn_xO_{35}$ (x = 0, 0.5, 1.0, 1.25, 1.5, and 3.0).

x	**0**	**0.5**	**1**	**1.25**	**1.5**	**3**
$a = b = c$ (Å)	15.0743(1)	15.0698(3)	15.0419(5)	15.0361(5)	15.0340(4)	14.9989(5)
V (Å^3)	3425.4(9)	3422.3(2)	3403.4(3)	3399.5(3)	3398.0(3)	3374.3(3)
Weighted R-profile (R_{wp}) and R-profile (R_p) factors for the S-XRD data histogram						
R_{wp} (%)	3.32	5.85	4.63	4.98	5.16	5.52
R_p (%)	2.16	3.79	3.18	3.41	3.53	3.85
Weighted R-profile (R_{wp}) and R-profile (R_p) factors for the NPD data histogram						
R_{wp} (%)	5.32	5.55	5.79	6.60	6.16	6.47
R_p (%)	4.18	4.37	4.44	4.97	4.83	5.09
Phase Fractions						
Main Phase (%)	100	100	100	100	100	92.4(2)
Ca_2MnO_4 (%)						7.6(2)

Table S4. Atomic parameters obtained from joint Rietveld refinements performed with the constraint of Mn content of $Ca_{14}Zn_6Ga_{10-x}Mn_xO_{35}$ (x = 0, 0.5, 1.0, 1.25,1.5, and 3.0).

***x* = 0**	**$Ca_{14}Zn_6Ga_{10}O_{35}$**						
Site	***x***	***y***	***z***	**Wyckoff Site**	**Occ**	**Beq (Å^2)**	**Atoms**
Ca1	**0.2130(2)**	**0**	**0**	**24*f***	**1**	**0.81(5)**	**24**
Ca2	**0.6128 (2)**	**0.6128 (2)**	**0.6128 (2)**	**16*e***	**1**	**0.47(4)**	**16**
Ca3	**0.3889(2)**	**0.3889(2)**	**0.3889(2)**	**16*e***	**1**	**0.47(4)**	**16**
Zn1	**0.1733(1)**	**0.1733(1)**	**0.1733(1)**	**16*e***	**1**	**0.36(3)**	**16**
Ga1	**0**	**0**	**0**	**4*a***	**1**	**0.58(9)**	**4**
Ga2	**−0.0009(2)**	**0.2500**	**0.2500**	**24*g***	**1**	**0.35(2)**	**24**
Ga3	**0.5000**	**0.5000**	**0.5000**	**4*b***	**1**	**0.27(9)**	**4**
Ga4	**0.8568(9)**	**0.8568(9)**	**0.8568(9)**	**16*e***	**0.5**	**0.36(3)**	**8**
Zn4	**0.8568(9)**	**0.8568(9)**	**0.8568(9)**	**16*e***	**0.5**	**0.36(3)**	**8**
O1	**0.2500**	**0.2500**	**0.2500**	**4*c***	**1**	**0.52(1)**	**4**
O2	**0.3663(2)**	**0**	**0**	**24*f***	**1**	**0.30(4)**	**24**
O3	**−0.0685(2)**	**−0.0685(2)**	**−0.0685(2)**	**16*e***	**1**	**1.65(7)**	**16**
O4	**0.0692(2)**	**0.2567(2)**	**0.3529(3)**	**48*h***	**1**	**0.76(2)**	**48**
O5	**0.1476(2)**	**0.2528(2)**	**0.5700(2)**	**48*h***	**1**	**0.76(2)**	**48**

x = 0.5			$Ca_{14}Zn_6Ga_{9.5(2)}Mn_{0.5(2)}O_{35}$				
Site	***x***	***y***	***z***	**Wyckoff Site**	**Occ**	**Beq (Å²)**	**Atoms**
Ca1	0.2121(2)	0	0	24*f*	1	1.29(9)	24
Ca2	0.6139(3)	0.6139(3)	0.6139(3)	16*e*	1	0.88(6)	16
Ca3	0.3875(3)	0.3875(3)	0.3875(3)	16*e*	1	0.88(6)	16
Zn1	0.1739(1)	0.1739(1)	0.1739(1)	16*e*	1	1.55(7)	16
Ga1	0	0	0	4*a*	1.000(17)	0.50(2)	4.000(68)
Ga2	−0.0015(4)	0.2500	0.2500	24*g*	0.989(6)	0.77(5)	23.736(144)
Mn2	−0.0015(4)	0.2500	0.2500	24*g*	0.011(6)	0.77(5)	0.264(144)
Ga3	0.5000	0.5000	0.5000	4*b*	0.629(15)	2.40(3)	2.516(60)
Mn3	0.5000	0.5000	0.5000	4*b*	0.371(15)	2.40(3)	1.484(60)
Ga4	0.8541(2)	0.8541(2)	0.8541(2)	16*e*	0.484(7)	1.55(7)	7.744(112)
Mn4	0.8541(2)	0.8541(2)	0.8541(2)	16*e*	0.016(7)	1.55(7)	0.256 (112)
Zn4	0.8541(2)	0.8541(2)	0.8541(2)	16*e*	0.5	1.55(7)	8
O1	0.2500	0.2500	0.2500	4*c*	1	0.35(1)	4
O2	0.3666(2)	0	0	24*f*	1	0.55(6)	24
O3	−0.0681(3)	−0.0681(3)	−0.0681(3)	16*e*	1	1.65(1)	16
O4	0.0706(4)	0.2555(4)	0.3542(4)	48*h*	1	1.36(4)	48
O5	0.1485(4)	0.2509(3)	0.5676(3)	48*h*	1	1.36(4)	48

x = 1.0		$Ca_{14}Zn_6Ga_{8.9(2)}Mn_{1.0(2)}O_{35}$					
Site	***x***	***y***	***z***	**Wyckoff Site**	**Occ**	**Beq (Å²)**	**Atoms**
Ca1	0.2130(2)	0	0	24*f*	1	1.43(1)	24
Ca2	0.6166(3)	0.6166(3)	0.6166(3)	16*e*	1	0.95(8)	16
Ca3	0.3876(3)	0.3876(3)	0.3876(3)	16*e*	1	0.95(8)	16
Zn1	0.1749(1)	0.1749(1)	0.1749(1)	16*e*	1	2.07(9)	16
Ga1	0	0	0	4*a*	0.956(16)	0.54(2)	3.824(64)
Mn1	0	0	0	4*a*	0.044(16)	0.54(2)	0.176(64)
Ga2	0.0012(4)	0.2500	0.2500	24*g*	0.994(6)	0.89(6)	23.856(144)
Mn2	0.0012(4)	0.2500	0.2500	24*g*	0.006(6)	0.89(6)	0.144(144)
Ga3	0.5000	0.5000	0.5000	4*b*	0.282(14)	2.40(4)	1.128(56)
Mn3	0.5000	0.5000	0.5000	4*b*	0.718(14)	2.40(4)	2.872(56)
Ga4	0.8488(2)	0.8488(2)	0.8488(2)	16*e*	0.449(7)	2.07(9)	7.184(112)
Mn4	0.8488(2)	0.8488(2)	0.8488(2)	16*e*	0.051(7)	2.07(9)	0.816(112)
Zn4	0.8488(2)	0.8488(2)	0.8488(2)	16*e*	0.5	2.07(9)	8
O1	0.2500	0.2500	0.2500	4*c*	1	0.48(1)	4
O2	0.3675(3)	0	0	24*f*	1	0.46(8)	24
O3	−0.0668(3)	−0.0668(3)	−0.0668(3)	16*e*	1	1.22(1)	16
O4	0.0709(3)	0.2543(4)	0.3600(3)	48*h*	1	1.15(6)	48
O5	0.1520(3)	0.2525(4)	0.5675(3)	48*h*	1	1.15(6)	48

x = 1.25	$Ca_{14}Zn_6Ga_{8.7(2)}Mn_{1.3(2)}O_{35}$						
Site	***x***	***y***	***z***	**Wyckoff Site**	**Occ**	**Beq (Å²)**	**Atoms**
Ca1	0.2130(2)	0	0	24*f*	1	1.32(8)	24
Ca2	0.6162(3)	0.6162(3)	0.6162(3)	16*e*	1	0.87(6)	16
Ca3	0.3875(3)	0.3875(3)	0.3875(3)	16*e*	1	0.87(6)	16
Zn1	0.1749(2)	0.1749(2)	0.1749(2)	16*e*	1	1.88(8)	16
Ga1	0	0	0	4*a*	0.886(13)	0.45(2)	3.544(52)
Mn1	0	0	0	4*a*	0.114(13)	0.45(2)	0.456(52)
Ga2	0.0018(4)	0.2500	0.2500	24*g*	0.989(5)	0.96(4)	23.736(120)
Mn2	0.0018(4)	0.2500	0.2500	24*g*	0.011(5)	0.96(4)	0.264(120)
Ga3	0.5000	0.5000	0.5000	4*b*	0.202(11)	0.90(3)	0.808(44)
Mn3	0.5000	0.5000	0.5000	4*b*	0.798(11)	0.90(3)	3.192(44)
Ga4	0.8479(2)	0.8479(2)	0.8479(2)	16*e*	0.429(6)	1.88(8)	6.864(96)
Mn4	0.8479(2)	0.8479(2)	0.8479(2)	16*e*	0.071(6)	1.88(8)	1.136(96)
Zn4	0.8479(2)	0.8479(2)	0.8479(2)	16*e*	0.50	1.88(8)	8
O1	0.2500	0.2500	0.2500	4*c*	1	0.30(1)	4
O2	0.3689(2)	0	0	24*f*	1	0.58(5)	24
O3	−0.0670(2)	−0.0670(2)	−0.0670(2)	16*e*	1	1.25(2)	16
O4	0.0697(3)	0.2543(4)	0.3588(3)	48*h*	1	1.28(3)	48
O5	0.1507(3)	0.2514(3)	0.5674(3)	48*h*	1	1.28(3)	48

x = 1.5	$Ca_{14}Zn_6Ga_{8.5(2)}Mn_{1.5(2)}O_{35}$						
Site	***x***	***y***	***z***	**Wyckoff Site**	**Occ**	**Beq (Å²)**	**Atoms**
Ca1	0.2135(2)	0	0	24*f*	1	1.44(9)	24
Ca2	0.6161(3)	0.6161(3)	0.6161(3)	16*e*	1	0.93(6)	16
Ca3	0.3872(3)	0.3872(3)	0.3872(3)	16*e*	1	0.93(6)	16
Zn1	0.1750(2)	0.1750(2)	0.1750(2)	16*e*	1	2.51(8)	16
Ga1	0	0	0	4*a*	0.878(13)	0.74(2)	3.512(52)
Mn1	0	0	0	4*a*	0.122(13)	0.74(2)	0.488(52)
Ga2	0.0018(4)	0.2500	0.2500	24*g*	0.972(6)	0.97(5)	23.328(144)
Mn2	0.0018(4)	0.2500	0.2500	24*g*	0.028(6)	0.97(5)	0.672(144)
Ga3	0.5000	0.5000	0.5000	4*b*	0.061(12)	0.90(2)	0.244(48)
Mn3	0.5000	0.5000	0.5000	4*b*	0.939(12)	0.90(2)	3.756(48)
Ga4	0.8458(2)	0.8458(2)	0.8458(2)	16*e*	0.432(7)	2.51(8)	6.912(112)
Mn4	0.8458(2)	0.8458(2)	0.8458(2)	16*e*	0.068(7)	2.51(8)	1.088(112)
Zn4	0.8458(2)	0.8458(2)	0.8458(2)	16*e*	0.50	2.51(8)	8
O1	0.2500	0.2500	0.2500	4*c*	1	0.55(14)	4
O2	0.3693(2)	0	0	24*f*	1	0.66(6)	24
O3	−0.0668(2)	−0.0668(2)	−0.0668(2)	16*e*	1	1.04(9)	16
O4	0.0699(3)	0.2543(4)	0.3585(3)	48*h*	1	1.35(4)	48
O5	0.1511(3)	0.2519(4)	0.5666(3)	48*h*	1	1.35(4)	48

x = 3.0	$Ca_{14}Zn_6Ga_{7.0(2)}Mn_{3.0(2)}O_{35}$						
Site	***x***	***y***	***z***	**Wyckoff Site**	**Occ**	**Beq (Å²)**	**Atoms**
Ca1	0.2145(2)	0	0	24*f*	1	1.26(8)	24
Ca2	0.6160(4)	0.6160(4)	0.6160(4)	16*e*	1	0.78(6)	16
Ca3	0.3866(4)	0.3866(4)	0.3866(4)	16*e*	1	0.78(6)	16
Zn1	0.1762(2)	0.1762(2)	0.1762(2)	16*e*	1	1.67(8)	16
Ga1	0	0	0	4*a*	0.596(14)	1.30(2)	2.384(56)
Mn1	0	0	0	4*a*	0.404(14)	1.30(2)	1.616(56)
Ga2	0.0025(5)	0.2500	0.2500	24*g*	0.872(6)	0.53(5)	20.928(144)
Mn2	0.0025(5)	0.2500	0.2500	24*g*	0.128(6)	0.53(5)	3.072(144)
Ga3	0.5000	0.5000	0.5000	4*b*	0.007(12)	1.20(2)	0.028(48)
Mn3	0.5000	0.5000	0.5000	4*b*	0.993(12)	1.20(2)	3.972(48)
Ga4	0.8384(2)	0.8384(2)	0.8384(2)	16*e*	0.291(7)	1.67(8)	4.656(112)
Mn4	0.8384(2)	0.8384(2)	0.8384(2)	16*e*	0.209(7)	1.67(8)	3.344(112)
Zn4	0.8384(2)	0.8384(2)	0.8384(2)	16*e*	0.5	1.67(8)	8
O1	0.2500	0.2500	0.2500	4*c*	1	0.48(2)	4
O2	0.3688(2)	0	0	24*f*	1	0.76(6)	24
O3	−0.0663(3)	−0.0663(3)	−0.0663(3)	16*e*	1	2.48(1)	16
O4	0.0692(4)	0.2519(5)	0.3556(4)	48*h*	1	1.74(4)	48
O5	0.1499(4)	0.2532(4)	0.5667(4)	48*h*	1	1.74(4)	48
Ca_2MnO_4							
O1	0	0	0.1600(5)	4*e*	1	1.50(13)	4
Ca1	0	0	0.3565(2)	4*e*	1	0.60(8)	4
O2	0	0.5	0	4*c*	1	1.40(2)	4
Mn1	0	0	0	2*a*	1	0.20(8)	2

Table S5. Spin Hamiltonian parameters calculated from the least-square fitting of EPR data for $Ca_{14}Zn_6Ga_{10-x}Mn_xO_{35}$ (x = 0.3, 0.5, 1.0, 1.25,1.5, and 3.0). g_x, g_y, and g_z are diagonal elements of the spectroscopic splitting matrix g, A is the hyperfine interaction matrix including diagonal elements A_x, A_y, and A_z, and D and E are axial and rhombic distortions, respectively, of the zero-field splitting (ZFS) parameters, D^{AB} is the general interaction matrix between A and B ions with spins S^A and S^B, respectively, with diagonal elements $D^{AB}{}_x$, $D^{AB}{}_y$, $D^{AB}{}_z$. The Curie–Weiss temperature T_{CW}, effective magnetic moment μ_{eff}, and the exchange interaction constant J were obtained from SQUID magnetometry data.

Sample	g $g_x = g_y = g_z$	ZFS parameters (cm^{-1})	A(mT) $A_x = A_y = A_z$	D^{AB} (mT) $D^{AB}{}_x = D^{AB}{}_y = D^{AB}{}_z$	T_{cw} (K)	μ_{eff} (μ_B)	$-J$ (cm^{-1})
x = 0.3	1.9965(2)	D = E ~ 0	7.16(2)	-	0.19(4)	3.68(3)	-
	1.991(1)	D = 0.0117(3) E = 0.00035(2)	-	68(5)			
x = 0.5	1.9965(2)	D = E ~ 0	7.16(2)	-	0.035(14)	3.62(1)	0.08 (2.28)
	1.991(1)	D = 0.0117(3) E = 0.00035(2)	-	69(5)			
x = 1.0	1.991(1)	D = 0.0126(3) E = 0.00035(2)	-	64(4)	−0.001(4)	3.15(1)	40(12)
x = 1.25	1.991(1)	D = 0.0126(3) E = 0.00035(2)	-	74(5)	−0.018(1)	3.07(1)	152(19)
x = 1.5	1.991(1)	D = 0.0118(3) E = 0.00035(2)	-	78(5)	−0.038(1)	3.02(1)	193(19)
x = 3.0	1.991(1)	D = 0.0057(3) E = 0.00035(2)	-	96(5)	−0.031(12)	2.91(2)	252(27)

Table S6. Parameters of Equations (10) and (11) for the thermal evolution of luminescence intensity were calculated from the non-radiative de-excitation of Mn^{4+} and Mn^{5+}. M_{orb} is the effective contribution to the electric dipole transition moment due to the collective action of all antisymmetric vibrational modes, $\hbar\omega$ is the effective phonon mode energy, E_{nr} and p_{nr} are the activation energy and frequency factor, respectively, for the non-radiative de-excitation process. τ_{so} is a spin–orbital interaction time related to the effect of the admixture of a higher excited state ($^4T_2$ in Mn^{4+} and $^3T_2$ in Mn^{5+}) –on the radiative probability of the spin-forbidden luminescent transition: $^2E \rightarrow {}^4A_2$ and $^1E \rightarrow {}^3A_2$ in Mn^{4+} and Mn^{5+}, respectively.

	Mn^{4+} **($^2E \rightarrow {}^4A_2$)**	**Mn^{5+}** **($^1E \rightarrow {}^3A_2$)**
τ_{so} (ms)	17.5±0.2	0.83±0.02
M_{orb}	5.8±0.6	0.08±0.01
$\hbar\omega$ (cm^{-1})	450±10	200±40
p_{nr}(s^{-1})	$(4.1\pm0.6)\cdot10^{10}$	$(1.26\pm0.09)\cdot10^{6}$
E_{nr} (cm^{-1})	5960±530	2200±130

Table S7. The fitted results of Pressure-dependent shift of x = 0.5 (Mn^{4+}) and x = 1.0 (Mn^{5+}) emissions. ZPL is the zero phonon line, $v1$ and $v2$ are visible phonon modes in Stokes phonon sidebands, and $v2'$ and $v1'$ in anti-Stokes phonon sidebands

	Mn^{4+} (x = 0.5)					**Mn^{5+} (x = 1.0)**
Phonon bands	ν1'	ν2'	ZPL	ν2	ν1	
Equation	y = a + b*x	y = a + b*x	y = a + b*x	y = a + b*x	y = a + b*x	y = a + b*x
Intercept	14764.68±4.60	14553.26±5.58	14419.69±21.47	14193.04±5.04	13964.08±15.01	8683.93±1.78
Slope	−3.8±0.1	−4.0±0.1	−4.1±0.2	−4.2±0.1	−3.8±0.1	−1.54±0.01
Adj. R^2	0.99	0.99	0.98	0.99	0.99	0.99

Supplementary references

(1) Liss, K. D.; Hunter, B.; Hagen, M.; Noakes, T.; Kennedy, S. Echidna—The New High-Resolution Powder Diffractometer Being Built at OPAL. *Physica B: Condensed Matter* **2006**, *385*, 1010–1012.

(2) Villars, P.; Cenzual, K. Pearson's Crystal Data: Crystal Structure Database for Inorganic Compounds (on DVD), Release 2021/22, ASM International®, Materials Park, Ohio, USA.

(3) Coelho, A. A. TOPAS and TOPAS-Academic: An Optimization Program Integrating Computer Algebra and Crystallographic Objects Written in C++. *J. Appl. Crystallogr.* **2018**, *51*, 210–218.

(4) Sears, V. F. Neutron Scattering Lengths and Cross Sections. *Neutron News* **1992**, *3*,

26–37.

(5) Momma, K.; Izumi, F. VESTA 3 for Three-Dimensional Visualization of crystal, Volumetric and Morphology Data. *J. Appl. Crystallogr.* **2011**, *44*, 1272–1276.

(6) Baur, W. The Geometry of Polyhedral Distortions. Predictive Relationships for The Phosphate Group. *Acta. Crystallogr. B. Struct. Sci. Cryst. Eng. Mater.* **1974**, *30*, 1195–1215.

(7) Kubicki, A. A.; Bojarski, P.; Grinberg, M.; Sadownik, M.; Kukliński, B. Time-Resolved Streak Camera System With Solid State Laser and Optical Parametric Generator in Different Spectroscopic Applications. *Opt. Commun.* **2006**, *263*, 275–280.

(8) Merrill, L.; Bassett, W. A. Miniature Diamond Anvil Pressure Cell for Single Crystal X-Ray Diffraction Studies. *Rev. Sci. Instrum.* **1974**, *45*, 290–294.

(9) Barzowska, J.; Lesniewski, T.; Mahlik, S.; Seo, H. J.; Grinberg, M. $KMgF_3:Eu^{2+}$ as a New Fluorescence-Based Pressure Sensor for Diamond Anvil Cell Experiments. *Opt. Mater.* **2018**, *84*, 99–102.

(10) Bain, G. A.; Berry, J. F. Diamagnetic Corrections and Pascal's Constants. *J. Chem. Educ.* **2008**, *85*, 532–536.

(11) Fang, M. H.; Wu, W. L.; Jin, Y.; Lesniewski, T.; Mahlik, S.; Grinberg, M.; Brik, M. G.; Srivastava, A. M.; Chiang, C. Y.; Zhou, W.; Jeong, D.; Kim, S. H.; Leniec, G.; Kaczmarek, S. M.; Sheu, H. S.; Liu, R. S. Control of Luminescence by Tuning of Crystal Symmetry and Local Structure in Mn^{4+}-Activated Narrow Band Fluoride Phosphors. *Angew. Chem. Int. Ed.* **2018**, *57*, 1797–1801.

(12) Liang, G.; Wu, Z.; Didier, C.; Zhang, W.; Cuan, J.; Li, B.; Ko, K.-Y.; Hung, P.-Y.; Lu, C.-Z.; Chen, Y.; Leniec, G.; Kaczmarek, S. M.; Johannessen, B.; Thomsen, L.; Peterson, V. K.; Pang, W. K.; Guo, Z. A Long Cycle-Life High-Voltage Spinel Lithium-Ion Battery Electrode Achieved By Site-Selective Doping. *Angew. Chem. Int. Ed.* **2020**, *59*, 10594–10602.

(13) Typek, J.; Wardal, K.; Zolnierkiewicz, G.; Leniec, G.; Sibera, D.; Narkiewicz, U. Magnetic Study of $ZnMnO_3$ in ZnO/MnO Nanocomposites. *IEEE Trans. Magn.* **2021**, *57*, 1–12.

(14) Rajendran, V.; Fang, M. H.; Huang, W. T.; Majewska, N.; Lesniewski, T.; Mahlik, S.; Leniec, G.; Kaczmarek, S. M.; Pang, W. K.; Peterson, V. K.; Lu, K. M.; Chang, H.; Liu, R. S. Chromium Ion Pair Luminescence: A Strategy in Broadband Near-Infrared Light-Emitting Diode Design. *J. Am. Chem. Soc.* **2021**, *143*, 19058–19066.

(15) Mombourquette, M.; Weil, J.; McGavin, D. EPR-NMR User's Manual. *Department of Chemistry, University of Saskatchewan, Saskatoon, SK, Canada* **1996**.

(16) Leniec, G.; Macalik, L.; Kaczmarek, S. M.; Skibiński, T.; Hanuza, J. EPR and Optical Properties of $KY(WO_4)_2:Gd^{3+}$ Powders. *J. Mater. Res.* **2012**, *27*, 2973–2981.

(17) Chalmin, E.; Farges, F.; Brown, G. E. A Pre-Edge Analysis of Mn K-edge XANES Spectra to Help Determine The Speciation of Manganese in Minerals and Glasses. *Contrib. Mineral. Petrol.* **2009**, *157*, 111–126.

(18) Yamamoto, T. Assignment of Pre-Edge Peaks in K-edge X-Ray Absorption Spectra of 3d Transition Metal Compounds: Electric Dipole or Quadrupole? *X-Ray Spectrom.* **2008**, *37*, 572–584.

(19) Jin, Y.; Fang, M. H.; Grinberg, M.; Mahlik, S.; Lesniewski, T.; Brik, M. G.; Luo, G. Y.; Lin, J. G.; Liu, R. S. Narrow Red Emission Band Fluoride Phosphor $KNaSiF_6:Mn^{4+}$ for Warm White Light-Emitting Diodes. *ACS Appl. Mater. Interfaces* **2016**, *8*, 11194–11203.